JGR Solid Earth

RESEARCH ARTICLE
10.1029/2023JB028170

Ultra-Low Velocity Zones Beneath the Southern Hemisphere Imaged With Double-Array Stacking of PcP Waveforms

Kayode J. Agboola[1,2], Samantha E. Hansen[1], Edward J. Garnero[3], Sebastian Rost[4], Mingming Li[3], and Sang-Heon Shim[3]

[1]Department of Geological Sciences, The University of Alabama, Tuscaloosa, AL, USA, [2]Now at Cornell University, Ithaca, NY, USA, [3]School of Earth and Space Exploration, Arizona State University, Tempe, AZ, USA, [4]School of Earth and Environment, The University of Leeds, Leeds, UK

Key Points:

- Core-reflected P-waves are used to investigate ultra-low velocity zones in the lowermost mantle beneath the southern hemisphere
- Results show widespread evidence for variable ultra-low velocity zones, some of which may indicate layered or gradational structure
- Variable accumulations of subducted oceanic crust with localized partial melting can explain these anomalous structures

Supporting Information:

Supporting Information may be found in the online version of this article.

Correspondence to:

S. E. Hansen,
shansen@geo.ua.edu

Citation:

Agboola, K. J., Hansen, S. E., Garnero, E. J., Rost, S., Li, M., & Shim, S.-H. (2024). Ultra-low velocity zones beneath the Southern Hemisphere imaged with double-array stacking of PcP waveforms. *Journal of Geophysical Research: Solid Earth*, *129*, e2023JB028170. https://doi.org/10.1029/2023JB028170

Received 31 OCT 2023
Accepted 4 APR 2024

Author Contributions:

Conceptualization: Kayode J. Agboola, Samantha E. Hansen, Edward J. Garnero, Sebastian Rost, Mingming Li, Sang-Heon Shim
Data curation: Kayode J. Agboola
Formal analysis: Kayode J. Agboola, Samantha E. Hansen
Funding acquisition: Samantha E. Hansen, Edward J. Garnero
Investigation: Kayode J. Agboola, Samantha E. Hansen, Edward J. Garnero
Methodology: Kayode J. Agboola, Samantha E. Hansen, Edward J. Garnero, Sebastian Rost, Mingming Li, Sang-Heon Shim
Project administration: Samantha E. Hansen, Edward J. Garnero
Software: Kayode J. Agboola, Samantha E. Hansen, Sebastian Rost, Mingming Li
Supervision: Samantha E. Hansen

Abstract Ultra-low velocity zones (ULVZs) are anomalous structures, generally associated with decreased seismic velocity and sometimes an increase in density, that have been detected in some locations atop the Earth's core-mantle boundary (CMB). A wide range of ULVZ characteristics have been reported by previous studies, leading to many questions regarding their origins. The lowermost mantle beneath Antarctica and surrounding areas is not located near currently active regions of mantle upwelling or downwelling, making it a unique environment in which to study the sources of ULVZs; however, seismic sampling of this portion of the CMB has been sparse. Here, we examine core-reflected PcP waveforms recorded by seismic stations across Antarctica using a double-array stacking technique to further elucidate ULVZ structure beneath the southern hemisphere. Our results show widespread, variable ULVZs, some of which can be robustly modeled with 1-D synthetics; however, others are more complex, which may reflect 2-D or 3-D ULVZ structure and/or ULVZs with internal velocity variability. Our findings are consistent with the concept that ULVZs can be largely explained by variable accumulations of subducted oceanic crust along the CMB. Partial melting of subducted crust and other, hydrous subducted materials may also contribute to ULVZ variability.

Plain Language Summary Earth's core-mantle boundary (CMB), the interface between the solid silicate mantle and the molten iron-rich outer core, is associated with a range of anomalous structures, including ultra-low velocity zones (ULVZs). While generally associated with reduced seismic wave velocities and sometimes increased density, prior studies have reported a wide range of ULVZ characteristics, leading to many questions regarding their origins. The lowermost mantle beneath the southern hemisphere provides a unique environment to study ULVZs because it is located away from regions of large-scale mantle upwelling and downwelling. Our study uses core reflected P-waves (PcP) recorded by seismic stations in Antarctica to investigate this portion of the CMB for ULVZ presence. We find widespread evidence for variable ULVZ structure. Some of the imaged ULVZs can be modeled with a single layer, but others are more complex. We suggest that the ULVZs beneath the southern hemisphere are predominantly associated with subducted oceanic crust that has variable accumulations along the CMB. In some regions, hydrated subducted materials may also experience partial melting, which may contribute to the complicated ULVZ structures imaged in some locations.

1. Introduction

The Earth's core-mantle boundary (CMB) represents a massive contrast in chemistry, viscosity, and material phase (e.g., Forte & Mitrovica, 2001; Knittle & Jeanloz, 1991; Lay, 1989; Lay et al., 2008; Loper & Lay, 1995; Ma et al., 2016; Ono et al., 2006; van der Hilst et al., 2007), making it a host to a variety of anomalous phenomena. One type of CMB structure of particular interest are ultra-low velocity zones (ULVZs): small-scale, laterally varying structures that have been imaged in some locations atop the CMB (Figure 1; e.g., Garnero & Helmberger, 1998; Garnero & Vidale, 1999; Williams et al., 1998). ULVZs are generally characterized by P- and S-wave velocity reductions (δV_P and δV_S) up to −25% and −50%, respectively (e.g., Brown et al., 2015; Idehara, 2011; Krier et al., 2021; Rondenay & Fischer, 2003; Rost et al., 2005) and, in some cases, increases in density ($\delta\rho$), up to +25% (e.g., Brown et al., 2015; Reasoner & Revenaugh, 2000), compared to the surrounding mantle. Further, ULVZs generally have thicknesses on the order of tens of kilometers (e.g., Brown et al., 2015; Idehara, 2011; Rost et al., 2005, 2010; Thorne & Garnero, 2004), but their lateral extents may be hundreds or even thousands of kilometers wide (e.g., Cottaar & Romanowicz, 2012; Jensen et al., 2013; Thorne et al., 2013; Wen & Helmberger, 1998; Yuan & Romanowicz, 2017). The highly variable range of ULVZ characteristics reported by

Validation: Kayode J. Agboola, Samantha E. Hansen
Visualization: Kayode J. Agboola, Samantha E. Hansen, Edward J. Garnero, Sebastian Rost, Mingming Li
Writing – original draft: Kayode J. Agboola
Writing – review & editing: Kayode J. Agboola, Samantha E. Hansen, Edward J. Garnero, Sebastian Rost, Mingming Li, Sang-Heon Shim

previous studies have led to many questions regarding the source of these anomalous structures and what role they may play in the chemical and thermal evolution of our planet.

Some studies have suggested that ULVZs are associated with thermal anomalies and partial melt along the CMB. This concept is motivated by the approximate 3:1 δV_S:δV_P ratio reported by some investigations (e.g., Berryman, 2000; Revenaugh & Meyer, 1997; Rost et al., 2006; Wen, 2000; Wen & Helmberger, 1998; Williams & Garnero, 1996) as well as by spatial correlations between regions displaying ULVZ evidence and the locations of hotspots (e.g., Cottaar & Romanowicz, 2012; Garnero et al., 1998; Garnero, 2000; Lai et al., 2022; Williams et al., 1998; Yuan & Romanowicz, 2017). Partial melting in the lowermost mantle could be promoted by high temperatures and the presence of volatiles along the CMB (e.g., Andrault et al., 2014; Cameron et al., 2003; Fan & Sun, 2021; Havens & Revenaugh, 2001; Nomura et al., 2014; Raddick et al., 2002; Steinberger & Holme, 2008). However, some ULVZs have been identified in presumed cooler regions of the lowermost mantle and do not display the characteristics associated with partial melt (e.g., Brown et al., 2015; Thorne & Garnero, 2004). This, coupled with plausibly higher ULVZ density, may indicate that ULVZs are compositionally distinct from the surrounding mantle. Such anomalies could, for instance, be generated by iron-enrichment (Kim et al., 2020; Knittle & Jeanloz, 1989; Lai et al., 2022; Z. Li et al., 2022; Liu et al., 2023; Mao et al., 2005, 2006; Nomura et al., 2011; Tanaka et al., 2020) or subducted materials above the CMB (Andrault et al., 2014; Dobson & Brodholt, 2005; Hansen et al., 2023; Li et al., 2017; Su et al., 2024; Wolf et al., 2024). Alternatively, fractional crystallization of a basal magma ocean (BMO), a remnant associated with an ancient compositional reservoir at the base of the mantle, has been suggested as the source of ULVZs (Boukare et al., 2015; Labrosse et al., 2007). It has also been suggested that ULVZs may be linked to the Large Low Velocity Provinces (LLVPs): two large-scale thermo-chemical anomalies in the mantle beneath Africa and the Pacific (Figure 1; e.g., Dziewonski et al., 1977; Garnero & McNamara, 2008; Hernlund et al., 2015). Geodynamic models (Brandenburg & Keken, 2007; Li, 2021; Li et al., 2017; McNamara et al., 2010; Mulyukova et al., 2015) suggest that lowermost mantle materials, including compositionally distinct ULVZs, could be swept toward areas of mantle upwelling, accumulating along the edges of the LLVPs.

Uncertainties regarding ULVZ origins are, in part, exacerbated by limited seismic sampling of the Earth's lowermost mantle. Until recently, only ~20% of the CMB had been investigated for ULVZ structure, with coverage of the deep mantle beneath the southern hemisphere being particularly sparse (Figure 1; e.g., Yu & Garnero, 2018). Large-scale studies, such as Thorne et al. (2020a, 2020b), have achieved ~60% CMB coverage with certain seismic phases, but ULVZ imaging beneath the southern polar region remains very limited. The CMB beneath the southern hemisphere is unique because it is away from the LLVPs and is not currently beneath active subduction zones; therefore, the presence and characteristics of ULVZs in this region may provide additional information about their origin. Several recent studies (Hansen et al., 2020, 2021, 2023) have significantly broadened ULVZ imaging south of about 30°S latitude (Figure 1). Most recently, Hansen et al. (2023) examined core-reflected P-waves (PcP) recorded by the Transantarctic Mountains Northern Network (TAMNNET; Figure 2) in Antarctica (Hansen et al., 2015) and found evidence for widespread ULVZ structure with variable thickness across the southern hemisphere. Additionally, geodynamic models presented in Hansen et al. (2023) suggested that ULVZs may be predominantly associated with subducted materials distributed throughout the lowermost mantle.

Building upon these prior investigations that explored limited portions of the southern hemisphere CMB (Hansen et al., 2020, 2021, 2023), the present study has the opportunity to expand ULVZ imaging even further by incorporating data from other Antarctic seismic stations. These broadly distributed stations (Figure 2), coupled with the abundance of seismic sources around Antarctica, both from subduction systems in the Pacific and from the circum-Antarctic ridge, allow us to investigate a larger portion of the CMB compared to earlier studies. Similar to Hansen et al. (2023), we focus on PcP waveforms that sample the lowermost mantle; however, we employ a different approach to evaluate the ULVZ structure since we must combine data from different seismic sources for our analysis. Specifically, we use the double-array stacking (DAS) technique (Avants et al., 2006; Hutko et al., 2009; Krüger et al., 1993; Revenaugh & Meyer, 1997) and synthetic waveform modeling to examine Antarctic-recorded PcP waveforms for ULVZ evidence. Our goal is to further evaluate the geographic distribution and variability of ULVZs beneath the southern hemisphere and to use the relative changes in ULVZ properties to explore possible processes that can generate this type of lowermost mantle structure. As part of this, our findings are also evaluated in relation to previously generated geodynamic models to further assess the

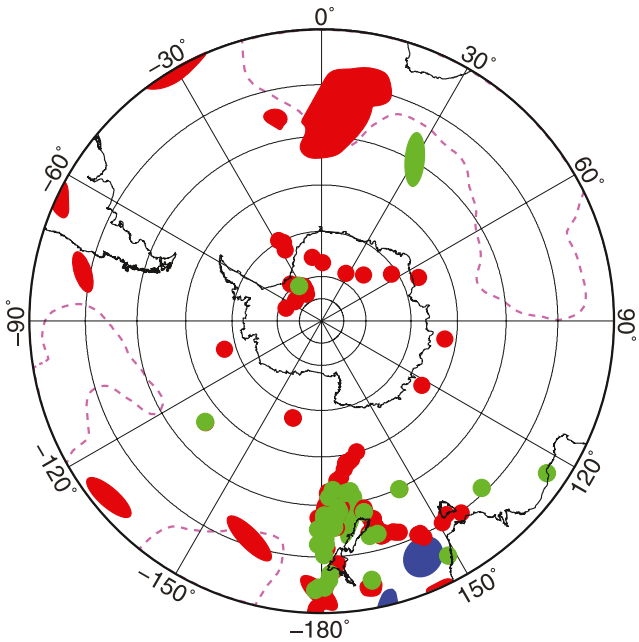

Figure 1. Map of prior ULVZ studies in the southern hemisphere. Red: ULVZ evidence found; Blue: no ULVZ evidence found; Green: uncertain ULVZ. Purple dashed lines denote LLVP boundaries. Modified from Yu and Garnero (2018) to include additional ULVZ regions from Hansen et al. (2020, 2023).

suggestion put forth by Hansen et al. (2023) that ULVZs can predominantly be associated with subducted materials.

2. Data and Methods

2.1. Data Collection, Pre-Processing, and Initial Stacking

Our ULVZ investigation incorporates PcP waveforms recorded by 238 three-component broadband seismic stations deployed across Antarctica (Figure 2; Table S1 in Supporting Information S1). PcP (Figure S1 in Supporting Information S1) is a useful seismic phase to examine the lowermost mantle structure because it samples a specific point on the CMB. If a ULVZ is present, the contrast in acoustic impedance between the ULVZ and the mantle above it results in a reflection off the top of the ULVZ, which is observed as a pre-cursory signal that arrives before the main PcP phase (e.g., Hansen et al., 2021, 2023; Hutko et al., 2009; Revenaugh & Meyer, 1997). PcP reverberations within the ULVZ can also generate post-cursory signals that arrive after PcP (Figure S1 in Supporting Information S1); however, the employed DAS technique (Section 2.5) focuses on PcP pre-cursors. Since the timing and amplitude of the pre-cursor depend on the ULVZ properties (i.e., thickness, δV_P, δV_S, $\delta\rho$), these phases can provide insight on the corresponding ULVZ structure (e.g., Hansen et al., 2021, 2023; Hutko et al., 2009).

We collected earthquakes with minimum magnitudes (M_w) of 5.0 and epicentral distances between 30° and 79° to avoid high PcP noise levels associated with the direct P-wave coda while also avoiding amplitude reduction caused by near-vertical incidence at the CMB (Persh et al., 2001). The imposed criteria resulted in 65,859 earthquakes recorded by the Antarctic stations. The data were pre-processed to remove the instrument response and were band-pass filtered between 0.50 and 1.50 Hz, an effective frequency range to study core-reflected P phases (e.g., Hansen et al., 2021, 2023; Rost et al., 2005). The waveforms were also rotated to their true longitudinal motion directions for P and PcP, and predicted arrival times for both phases were determined using the Preliminary Reference Earth Model (PREM; Dziewonski & Anderson, 1981) as well as the TauP toolkit (Crotwell et al., 1999).

Initial, linear stacks were generated for each event with the waveforms aligned on their PREM-predicted P arrival times. While PcP phases are the main focus of our study, P-wave arrivals have larger amplitudes, and therefore generally higher signal-to-noise ratios (SNRs), compared to PcP. This is because PcP phases travel longer paths through the mantle and thus experience higher attenuation. Also, a significant portion of the P energy at the CMB continues into the outer core as a PKP wave, which ultimately reduces the amplitude of the PcP reflection. Given this, we initially focused our analyses on P-wave arrivals to identify the best quality waveforms because if the P-wave signal is robust, then there is a better possibility of identifying PcP. Two SNR measurements were made for each trace: one using a noise window defined from 30 to 15 s prior to the P arrival (SNR_{before}) and the other with the noise window 10–25 s after the P signal (SNR_{after}; the signal window was defined from 5 s before to 10 s after P). Similar SNR measurements were also made for the linear P-wave stack. If an event had at least three P waveforms with both SNR_{before} and $SNR_{after} \geq 2$, or if both SNR measurements for the linear stack were ≥2, the event was retained for our analysis. Otherwise, it was discarded. This approach was taken to focus on events with impulsive P-wave arrivals that were not dominated by large-amplitude depth phases. We note that we also checked whether PcP was predicted to arrive within the SNR_{after} noise window. If so, the waveform was retained, provided that PcP was also sufficiently separated from any depth phases (by at least 8 s). Of the original 65,859 events, 4,736 earthquakes met the P-wave SNR criteria, and this data set formed the base for further analysis (Figure 2).

Following the approach of Hansen et al. (2021), the linear P-wave stacks for a given event were then cross-correlated with each of the corresponding, individual P waveforms to determine delay times and cross-correlation coefficients (CCCs). The individual waveforms were time-shifted by their delay times to improve the alignment of the P signal, and each waveform was weighted by its CCC^2 value as well as a weight based on the waveform's SNR ($W_{P\text{-}SNR}$; Text S1 in Supporting Information S1; Hansen et al., 2021). The realigned, weighted

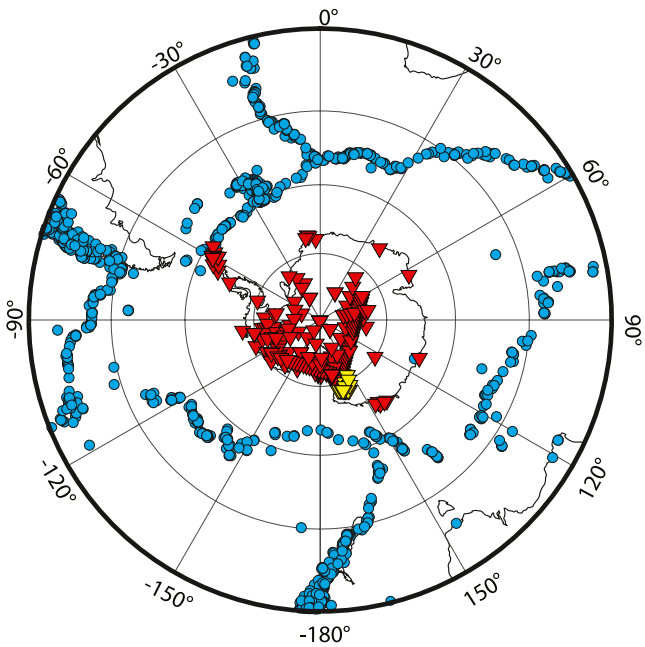

Figure 2. Antarctic stations and seismic events. Triangles denote the locations of the 238 Antarctic seismic stations used in this study, with TAMNNET stations (Hansen et al., 2015) highlighted in yellow and stations from other networks shown in red. Blue dots denote the 4,736 earthquakes that met our P-wave SNR criteria, described in Section 2.1.

waveforms were then restacked, and this process was repeated until the CCC between the most recent stack and the previous one was greater than 0.995. This procedure improves the alignment of the individual waveforms and generates a representative P-wave stack for each event (Hansen et al., 2021).

2.2. Historical Interstation Pattern Referencing and Restacking

The time-shifts applied to the waveforms described in Section 2.1 may vary significantly for different earthquakes, even when those events are recorded by the same station. This could result from structural variability between the earthquake and the station, event mislocation errors, and/or small-scale structure beneath the station. The source(s) of absolute time-shift variations between individual records typically cannot be identified; however, it is important to determine if the applied time shifts are robust. We used the Historical Interstation Pattern Referencing (HIPR) method developed by Hansen et al. (2021) to evaluate the time shifts applied to our data and to develop associated event ($HIPR_{EVT}$) and station ($HIPR_{STA}$) weights (see Text S2 in Supporting Information S1). Higher values of $HIPR_{EVT}$ and $HIPR_{STA}$ correspond to more reliable time-shifts (i.e., ones that are more similar to historical patterns; Hansen et al., 2021), and Figure S2 in Supporting Information S1 summarizes the $HIPR_{EVT}$ and $HIPR_{STA}$ values for our data set.

The HIPR weights were then incorporated into a stacking approach similar to that discussed in Section 2.1. Like before, each P waveform was weighted by its $W_{P\text{-}SNR}$ and CCC^2 values, but now the $HIPR_{EVT}$ and $HIPR_{STA}$ weights were also applied (Hansen et al., 2021, 2023). The iterative stacking approach was reapplied to each event in the data set to create updated and optimized P-wave stacks (Figure 3). The goal of this restacking is two-fold. First, robust P-wave stacks are required for data deconvolution, a processing step that will be described in Section 2.3. Second, PcP arrival times need to be assigned to each event-station record.

The PcP waveforms were time shifted by the same amount as their corresponding P waveforms. Also, the observed P-wave arrival time from the optimized stack, along with the PREM-predicted PcP-P time, were used to assign PcP arrival times to each waveform. That is, it is assumed that the PcP-P time from PREM is the same as the PcP-P time in the actual data, meaning that if an observed P-wave arrives early (or late) compared to its PREM-predicted time, the corresponding PcP arrival will also be early (or late) by the same amount. As discussed in Section 2.1, the amplitude of PcP is often small, making it difficult to identify on individual waveforms; therefore, the described approach allows PcP arrival times to be assigned even if the phase itself has a low SNR. We acknowledge that velocity variations, particularly in the lowermost mantle, can lead to PcP arrival time variance. However, we examined the PcP-P deviations from PREM for several tomographic models (Lei et al., 2020; Simmons et al., 2021), and their differences are fairly small (averaging ~0.5 s). Additionally, as discussed in Section 2.4 below, the PcP waveforms are geographically grouped, so any lower mantle structure that may affect the PcP arrival time will plausibly affect all the waveforms in a given group. Therefore, PcP arrival time uncertainty does not strongly influence our analysis.

2.3. Deconvolution

Since PcP signals from different earthquakes need to be stacked to investigate ULVZ structure beneath the southern hemisphere, the waveforms must be source-equalized (e.g., Avants et al., 2006; Hutko et al., 2009). For each event, we extracted a source wavelet (i.e., a sample of energy representing the earthquake source) from the HIPR-based P-wave stack using a 25 s window centered on the P-wave arrival, and the wavelet was deconvolved from the corresponding, individual P waveforms using water-level deconvolution (Ammon, 1991; Langston, 1979). A suite of water-level values, Gaussian filter widths, and high-pass filter limits were tested for our data set. The water-level helps to prevent the deconvolved traces from being dominated by noise, which can result from low amplitudes in the denominator during spectral division when the deconvolution is performed. The

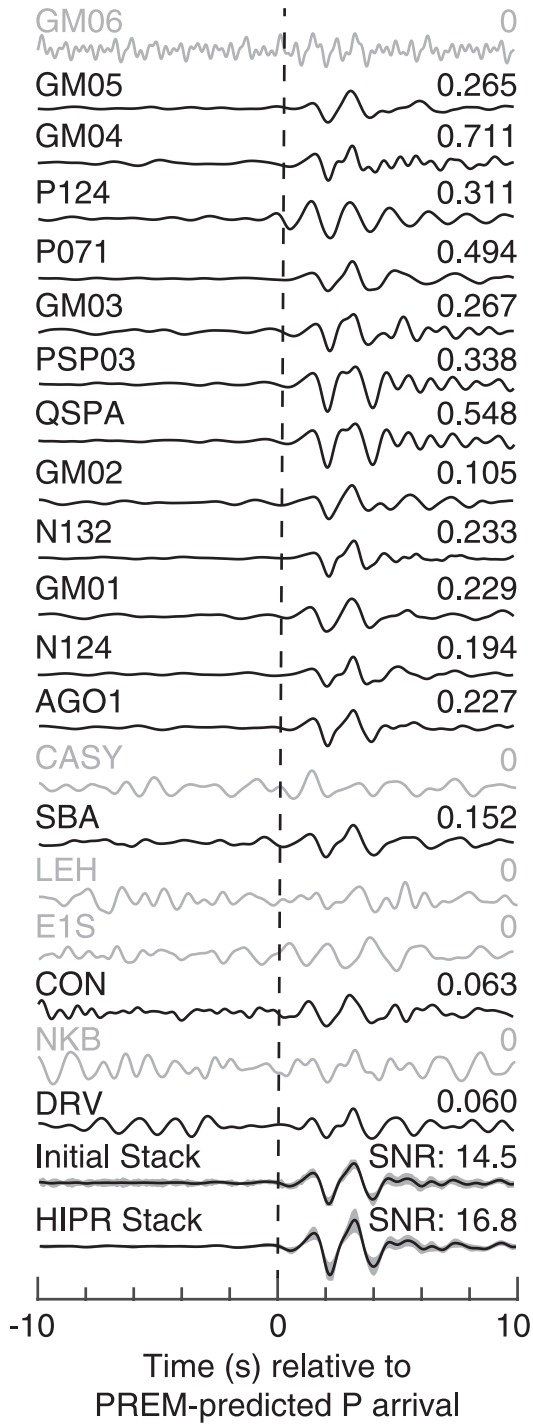

Figure 3. Example weighted P waveforms and stacks. The individual P waveforms are labeled with their corresponding station names (left) and their total, HIPR-based weights (right). Gray shading on the stacks (bottom two traces) indicates one standard deviation, and the corresponding reported values are the stack SNRs. The initial stack is that described in Section 2.1. Gray traces were removed during the final stacking process (Section 2.2) and are not included in the HIPR stack. All waveforms correspond to an event that occurred on 7 January 2009 (16:25:33.43).

Gaussian filter removes high frequency noise from the data, and its frequency content is controlled by its filter-width (Ammon, 1991). Similarly, high-pass filtering was applied to mitigate low-frequency variations in the data.

Applied water-level values were allowed to vary from 0.00001 to 0.5, the Gaussian filter width was varied from 1.0 to 10.0, and the high-pass filter limit was varied from 0.1 to 1.3 Hz. We also explored omitting the Gaussian and high-pass filter. Each parameter combination was used to deconvolve the extracted source wavelet from each of the P waveforms for a given event. Then, a weighted, deconvolved P-wave stack was generated using the same weights described in Section 2.2. A corresponding deconvolution SNR was also computed by defining a signal window around the P-wave peak on the stack, with noise windows to either side (Figure S3 in Supporting Information S1). The best set of deconvolution parameters (i.e., water-level, Gaussian filter width, and high-pass filter limit) were those whose combination led to the highest deconvolution SNR. For our data set, events with deconvolution SNR values ≥ 15 displayed high-quality, deconvolved P-wave stacks and hence were assigned a deconvolution-related weight (W_{DECON}) of one (Figure S3 in Supporting Information S1). Conversely, events with deconvolution SNR values ≤ 7 were generally associated with low-quality signals and were assigned W_{DECON} of 0.05 (Figure S3 in Supporting Information S1). Events with deconvolution SNR values between 15 and 7 were assigned a W_{DECON} with a linear ramp function (between 1 and 0.05). The best set of deconvolution parameters for a given event were then applied to all the corresponding PcP records. All 4,736 events in our data set were deconvolved in this manner.

2.4. Binning and PcP Waveform Weighting

The southern hemisphere study area was divided into geographic bins using a $2° \times 2°$ grid and a moving, circular bin with a radius of 2°. This approach provides some overlap between adjacent bins. Since lines of longitude converge near Antarctica, the bins were defined in a rotated coordinate system, where the South Pole was situated on the equator (Figure S4 in Supporting Information S1). This was done to ensure the bins have equal area and consistent overlap. The PcP CMB reflection (bounce) points were also rotated in the same manner, and any bounce points that fell into a given bin were grouped together. This resulted in 1,933 non-empty bins. Additionally, within each bin, a distance-from-bin-center weight (W_{DIST}) was determined for each PcP CMB bounce point. Records with bounce points at the bin center were given a W_{DIST} of 1.0, while those at the edge of the bin were given a W_{DIST} of 0.5. The distance weighting was applied to accommodate non-uniform bin sampling, especially when the PcP waveforms predominately sample the bin edges. That said, given the small size of our bins and the largely overlapping PcP Fresnel zones within them, the effect of this weighting is minor. All bins and bounce points were then rotated back to true coordinates (Figure S5 in Supporting Information S1).

Ultimately, each event-station PcP waveform had six different weights applied, which were multiplied together to generate a corresponding composite weight (compWeight), as defined by Equation 1.

$$\text{compWeight} = \text{HIPR}_{EVT} \cdot \text{HIPR}_{STA} \cdot W_{P-SNR} \cdot W_{PcP-SNR} \cdot W_{DECON} \cdot W_{DIS}T \quad (1)$$

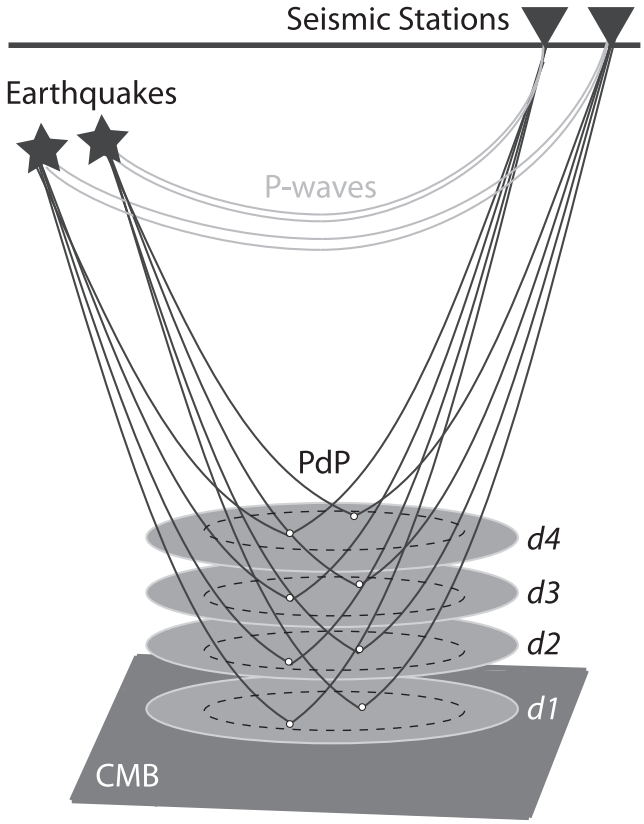

Figure 4. Double-array stacking technique. Cartoon illustrates the applied methodology. Gray ellipses represent target reflectors above the CMB at positions *d1*, *d2*, etc. For a given bin (dashed black ellipses), all PdP reflection points at a given target depth are stacked, and the corresponding amplitude is assessed for potential ULVZ presence. Modified from Hutko et al. (2009).

In Equation 1, $HIPR_{EVT}$ and $HIPR_{STA}$ are the HIPR-based event and station weights, respectively. We note that each PcP waveform inherited its HIPR weights from its corresponding P record. $W_{P\text{-}SNR}$ and $W_{PcP\text{-}SNR}$ are weights assigned based on the SNR of the P and PcP waveforms, respectively (see Text S1 in Supporting Information S1). W_{DECON} is the deconvolution-related weight described in Section 2.3, and W_{DIST} is the weight associated with a record's PcP CMB bounce point distance from the center of the bin. This weighting scheme not only generates robust PcP stacks but also allows high-quality PcP records to more strongly constrain the DAS analysis, which is described in Section 2.5.

2.5. Double-Array Stacking

The DAS technique (Figure 4; Avants et al., 2006; Hutko et al., 2009; Reasoner & Revenaugh, 1999; Revenaugh & Meyer, 1997) was applied to probe the CMB beneath the southern hemisphere for ULVZ structure. This method combines PcP signals that have CMB reflections within a given bin to create a suite of 1-D depth-profile stacks (Figure 4). If the top of a ULVZ is present at some position above the CMB, the stack corresponding to that depth (d) should display a coherent reflected PcP pre-cursor (PdP). Conversely, a lack of coherent signal in the stack can either indicate that no ULVZ is present or that it cannot be resolved.

Several additional processing steps and quality control criteria were applied to our data prior to stacking. The frequency content of our P and PcP waveforms may have been altered by the applied deconvolution (Section 2.3), even though they were initially bandpass-filtered between 0.5 and 1.5 Hz (Section 2.1); therefore, similar to Hutko et al. (2009), we examined several additional filtering options. Specifically, a band-pass filter between 0.25 and 0.5 Hz as well as high-pass filters with cut-off frequencies of 0.25 and 0.50 Hz, respectively, were tested. Both the band-pass filter and the 0.50 Hz high-pass filter smoothed and broadened the P and PcP signals too heavily, resulting in loss of detail in the associated stacks. The 0.25 Hz high-pass filter, on the other hand, generally led to better results with clear P and PcP signals (Figure S6 in Supporting Information S1); therefore, this filtering option was applied to our full data set.

For an individual seismic record to be included in the PcP double-array stack, minimum SNR values of 0.8 and 3 were required for the PcP and P waveforms, respectively (Figure S7 in Supporting Information S1). These SNR thresholds were determined from visual inspection and were imposed to promote the highest quality data. Additionally, to ensure our analysis was focused on the pre-cursory phases of interest, the arrival times of potentially interfering seismic phases (pP, sP, PP, pPP, sPP) relative to the PcP arrival time were determined using PREM (Dziewonski & Anderson, 1981). Given the event depths and distances in the examined data set, as well as the range of ULVZ heights relative to the CMB that we examined (see below), it was estimated that the reflected PdP signal of interest could arrive up to about 7 s earlier or 3 s later than the predicted PcP time. Therefore, we conservatively discarded any waveforms with other seismic phases predicted to arrive within 8 s prior or 4 s after PcP.

The radiation pattern of an earthquake can sometimes lead to opposite P and PcP polarities. Since centroid moment tensors (CMTs) are generated for long-period seismic waves (Dziewonski et al., 1981; Ekström et al., 2012), it is challenging to use CMTs to predict such polarity differences for the short-period (1 Hz) data we are examining. Therefore, we took the envelope of each deconvolved PcP record to remove any potential polarity uncertainty. The enveloped PcP records were normalized to set their maximum amplitudes to 1.0, they were aligned on their predicted PcP arrival times (Section 2.2; Figure S8 in Supporting Information S1), and a corresponding weighted stack was generated for each bin, where the composite weights (Section 2.4) were applied to each respective waveform. The stack amplitude at 0 s, which corresponds to the predicted PcP arrival time, represents the strength of the reflection from the CMB.

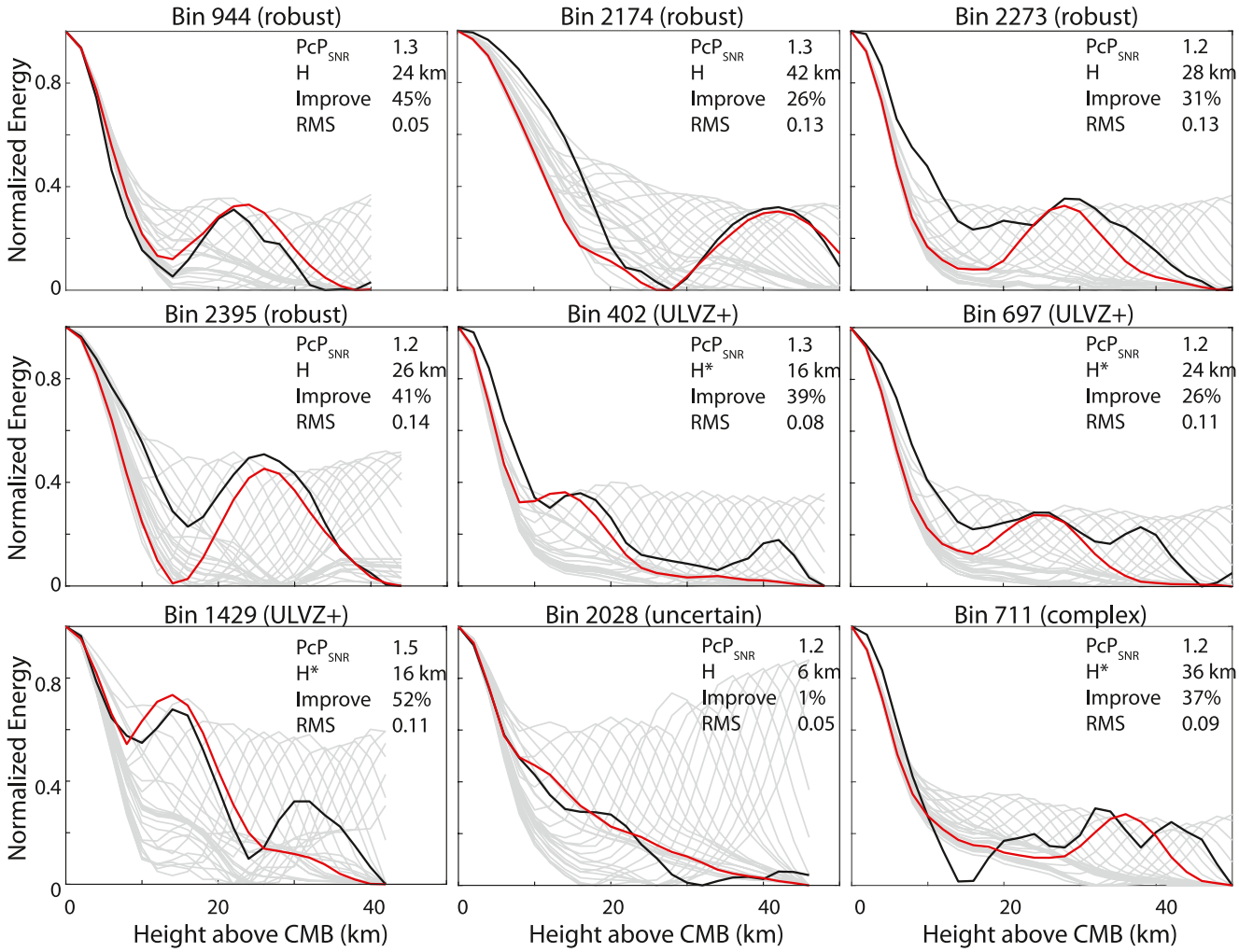

Figure 5. Examples of double-array stacking results. Each panel corresponds to one of the geographic bins examined in our study. Black lines show the observed double-array stack, while red and gray lines denote the synthetic results for each tested ULVZ thickness. The red line highlights the best-fit synthetic based on the RMS error. The corresponding PcP-stack SNR (PcP_{SNR}), the best-fit ULVZ thickness (H), the percent improvement in fit compared to PREM (Improve), and the best-fit RMS error (RMS) are also listed. ULVZ thicknesses for ULVZ+ and complex bins (H*) are not interpreted but are included for completeness. The plots for some bins are truncated as a result of repositioning the PcP reflection at the CMB (0 km), as discussed in Section 3.2.1.

Target depths ranging from 20 km below to 50 km above the CMB in 2 km increments were examined for each bin. For a given target depth, the corresponding predicted PdP arrival time was computed using a modified version of PREM that included a ULVZ with δV_P, δV_S, and $\delta\rho$ of −10%, −30%, and +10%, respectively. These initial choices for the ULVZ parameters were selected because they are some of the most commonly reported characteristics suggested by previous studies (e.g., Bower et al., 2011; Rost et al., 2006; Williams & Garnero, 1996; Yu & Garnero, 2018). The PcP waveforms in the examined bin were then time-shifted to align them on their predicted PdP times, and a corresponding weighted stack was again determined. The amplitude at the alignment time was also recorded. As noted previously, if a ULVZ is present, a coherent PdP reflection from the top of the layer will result in a higher amplitude signal in the stack. Conversely, if no ULVZ is present, destructive interference will result in a lower stack amplitude (Hutko et al., 2009).

3. Results

The DAS results for each bin are summarized by plots of ULVZ thickness versus reflection amplitude, where the amplitude of the PcP peak is normalized to one. Examples are shown in Figure 5 and Figure S9 in Supporting Information S1. All results were visually inspected to assess the coherence and reliability of the double-array

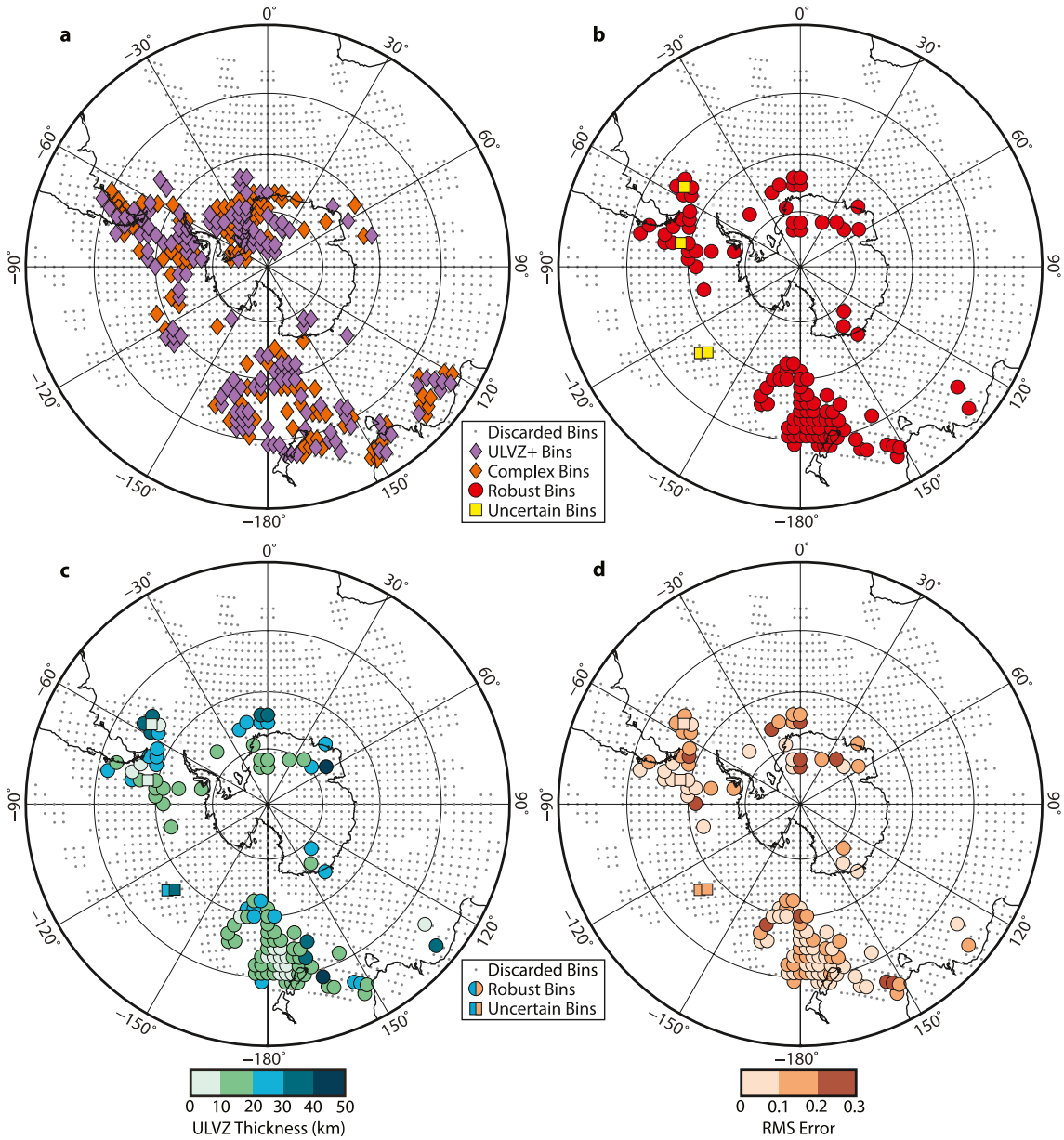

Figure 6. Summary of ULVZ results. (a) Purple diamonds denote the 149 "ULVZ+" bins, and orange diamonds denote the 103 "complex" bins. Gray dots indicate the 1,569 bins that were dismissed either because they contained less than 20 PcP bounce points or because their PcP SNR < 1.2. (b) Similar to (a) but now showing the 108 "robust" (red circles) and 4 "uncertain" (yellow squares) bins. (c) Same as (b) but now the "robust" (circles) and "uncertain" (squares) bins are color-coded by their corresponding best-fit ULVZ thicknesses (assuming $\delta V_P = -10\%$, $\delta V_S = -30\%$, and $\delta\rho = +10\%$). (d) Same as (c) but now colors correspond to RMS errors.

stacks. For instance, if the PcP reflection from the CMB was unclear (i.e., had a low SNR), then the corresponding PdP results are likely unreliable, and results for such bins were discarded. From our assessment, we decided that only bins with 20 or more PcP event-station records would be considered. Additionally, the generated bin stacks were required to have PcP signals with a SNR $\geq$ 1.2. These criteria help to ensure that our ULVZ investigation is based on the most robust double-array stacks. Of the original 1,933 geographic bins (Figure S5 in Supporting Information S1; Section 2.4), 364 bins met these requirements. This corresponds to a reduction of about 80% (Figure 6).

3.1. Synthetic Modeling

To further characterize the ULVZ thicknesses determined from the DAS, 1-D synthetic modeling was employed. The generalized ray method of Gilbert and Helmberger (1972) was used to generate synthetic spike trains that correspond to each event-station record in the data set. All synthetic signals were generated with the same ULVZ parameters (i.e., $\delta V_P = -10\%$, $\delta V_S = -30\%$, and $\delta\rho = +10\%$) used in the DAS analysis (Section 3), but the ULVZ thickness was varied from 0 to 50 km with an increment of 2 km. The synthetic spike trains created for each ULVZ model only include PcP and the ULVZ-associated pre- and post-cursors; they do not contain the direct P-wave nor any other potentially interfering seismic phases. For each considered event, a P-wavelet was extracted from the deconvolved P-wave stack using a ±3 s window around the P peak, and this P-wavelet was convolved with the synthetic spike trains to create synthetic PcP records for each recording station. The individual synthetic PcP waveforms were then filtered and processed with the same DAS procedure as that applied to the observed data. It is worth noting that the composite weights needed to make the weighted, synthetic PcP stacks were inherited from the corresponding true waveforms. For a given bin, the synthetic DAS results were compared to the actual results by computing the root-mean-square (RMS) error between them. A lower RMS error indicates a better match between the observed and synthetic data (Figure 5; Figure S9 in Supporting Information S1). We also determined the percent improvement in fit for the best-fit synthetic model compared to PREM (i.e., a non-ULVZ-inclusive model). Our approach allows a broad suite of ULVZ models to be evaluated, which is not feasible with more complex, computationally demanding modeling techniques (e.g., Jenkins et al., 2021; J. Li et al., 2022; Z. Li et al., 2022).

All of the modeled bins were visually inspected to evaluate the coherency and robustness of any ULVZ precursory signal from the DAS as well as the fit of the corresponding synthetics, and our results were classified into four categories. First, bins that clearly displayed ULVZ-indicative signals, had good matches between their 1-D synthetics and observations, and whose best-fit ULVZ model fit the DAS results at least 10% better than PREM were classified as "robust." Second, even if a given bin did not clearly display ULVZ evidence, we cannot rule-out the possibility of a ULVZ since the structure may be too thin to resolve. Therefore, if a bin was well-matched by its synthetic but the percent improvement in fit compared to PREM was less than 10%, the bin was classified as "uncertain." Third, in a number of cases, the DAS results showed two distinct PdP peaks that could not be matched by the 1-D synthetic modeling, and this may suggest layered ULVZ structure or some other type of lowermost mantle heterogeneity. Such bins were given the classification of "ULVZ+." Fourth, bins with DAS results showing multiple peaks were put into the "complex" category. Of the 364 modeled bins, 108 were classified as robust, 4 were classified as uncertain, 149 were classified as ULVZ+, and the remaining 103 were complex. Our bin classification is summarized in Figure 6 and in Tables S2–S4 in Supporting Information S1. Tables S5 and S6 in Supporting Information S1 also provide the average and standard deviation of the RMS misfit as well as the percent improvement in fit compared to PREM for the different groups of bins described previously. Generally, as the bins are honed, as described in both Section 3 and in this section, the RMS error decreases and the fit between the synthetics and the observed data improves. Our results (Figure 6; Figure S10 in Supporting Information S1) indicate a wide range of ULVZ thicknesses across the southern hemisphere, with evidence for multi-layer or complicated ULVZ structure in many locations. Conservatively, 71% of the modeled bins have double-array stacks that are better explained by the presence of some type of ULVZ, though the actual percentage is likely higher since some of the complex bins are also likely associated with ULVZ structure.

3.2. Uncertainty Assessment

Our ULVZ thickness estimates depend on several modeling assumptions. First, as described in Section 2.5, the DAS was performed using a modified version of PREM (Dziewonski & Anderson, 1981) that includes a ULVZ. For some bins, the PcP peak did not align with the CMB (i.e., at 0 km relative depth) as expected. This could be caused by lower mantle seismic velocity variations compared to PREM (Hutko et al., 2009; Shearer & Flanagan, 1999; Trampert et al., 2001). Alternatively, the P or PcP waves could have encountered velocity anomalies in the mid-mantle that were not sampled by the other phase. Such velocity anomalies could affect the corresponding travel times, which, in turn, could affect the differential PcP-P timing. Given this, we generated additional double-array stacks to assess the uncertainty associated with the assumed velocity structure (Section 3.2.1).

Additionally, as discussed in Sections 2.5 and 3.1, the DAS and synthetic modeling were performed assuming a ULVZ with $\delta V_P = -10\%$, $\delta V_S = -30\%$, and $\delta\rho = +10\%$. However, trade-offs between ULVZ thickness and

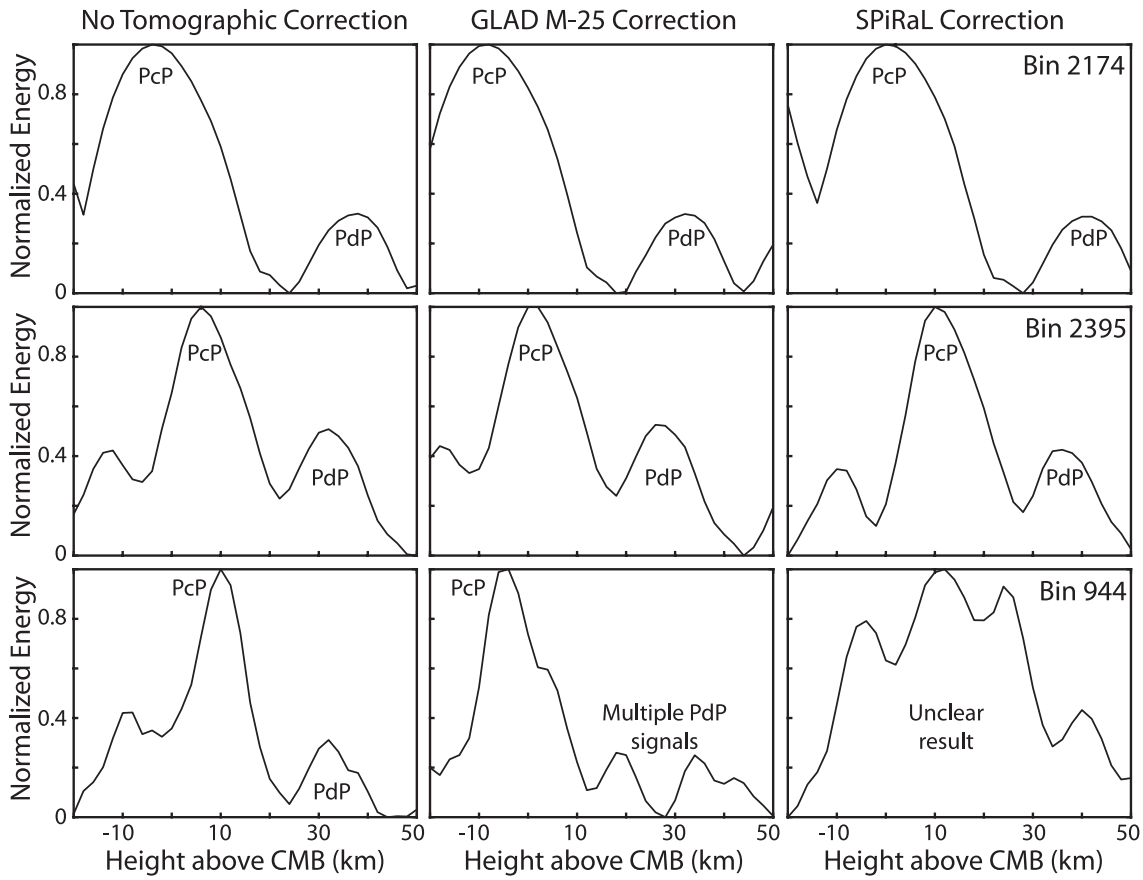

Figure 7. Tomographic timing corrections. DAS results are shown for three example robust bins (rows). The first column shows the original results obtained without tomographic corrections applied. The second column shows the results with GLAD-M25 (Lei et al., 2020) tomographic timing corrections applied, and the third column shows the results with SPiRaL (Simmons et al., 2021) tomographic timing corrections applied. Note how the PcP peaks in the first column are not positioned at the CMB (0 km). In the top row, the SPiRaL timing corrections improved this bin's results and aligned the PcP peak at the CMB. In the middle row, the GLAD-M25 timing corrections improved the bin's results. In the bottom row, both sets of tomographic timing corrections worsened the bin's results and complicated the double-array stack, which may indicate that the approach is now stacking noise instead of coherent, aligned signals.

velocity reduction are common in 1-D modeling (Garnero & Helmberger, 1998; Garnero & Jeanloz, 2000; Hansen et al., 2023; Thorne & Garnero, 2004). That is, a thinner ULVZ with a larger velocity reduction may plausibly fit the observed data equally well as a thicker ULVZ with a lower velocity reduction. Therefore, we also evaluated how our ULVZ thicknesses depend on the assumed δV_P, δV_S, and $\delta\rho$ values (Section 3.2.2).

It has also been suggested that ultra-high velocity zones (UHVZs) may exist along the CMB as well (e.g., Yu et al., 2018; Garnero et al., 2020; Pachhai et al., 2022b). The PdP reflection from this type of structure could potentially look similar to the ULVZ DAS results since the difference in polarity is removed when the PcP waveforms are enveloped (Section 2.5). Therefore, we performed several additional tests to ensure that our results are indicative of ULVZ structure (Section 3.2.3).

3.2.1. Timing Corrections

While the actual velocity structure inside the Earth is not exactly known, it may be approximated by 3-D seismic tomography models. Given this, two recent global P-wave velocity models, GLAD-M25 (Lei et al., 2020) and SPiRaL (Simmons et al., 2021), were both used to determine phase arrival time corrections. The timing corrections were computed using ray paths predicted by PREM (Dziewonski & Anderson, 1981), and the velocities at various positions along each ray path were extracted from the tomographic model of interest. For a given event-station record and a given phase (P or PcP), the cumulative travel-time residual between the 3-D velocity model and the 1-D PREM reference model was determined over the full ray path. A differential travel-time residual

between PcP and P was then computed, which was added to the predicted PcP arrival time to apply the tomographic correction. While the examined ray paths are not truly 3-D, heterogeneity in the tomographic models is long wavelength, and our differential phase analysis helps to reduce associated uncertainties while also providing a computationally convenient approach to determine the travel-time perturbations over the large ULVZ parameter space we are exploring.

Once the tomographic timing corrections were applied, the DAS procedure and synthetic modeling were repeated to assess if there were any notable changes in our results related to the assumed velocity structure (see Tables S5 and S6 in Supporting Information S1). The tomographic timing corrections improved the DAS results for about 23% of the examined bins, correctly positioning the PcP reflection at the CMB and/or leading to improved PdP signals (Figure 7). However, neither GLAD-M25 nor SPiRaL consistently outperformed the other. For the remaining 77% of the examined bins, the applied tomographic corrections did not notably improve the results, or they led to unclear findings when compared to the original approach (Figure 7). Generally, whether the tomographic corrections were applied or not, the average RMS error and the average fit between the data and the synthetics were not significantly different (Tables S5 and S6 in Supporting Information S1). The uncertainty in Earth's true velocity structure is difficult to quantify; therefore, we took an approach similar to Hutko et al. (2009) and any DAS result whose PcP peak was shifted away from the CMB was adjusted to correctly position this reflection. We note that all double-array ULVZ thicknesses had to be reduced to perform this adjustment when the PcP peak was at a positive height above the CMB, which causes the corresponding plots to shift to the left. Examples of this can be seen in Figure 5. Such corrections were typically small, averaging about 5 km, but this uncertainty does influence the obtained ULVZ thicknesses. The results shown in Figure 6 take these PcP time shifts into account for bins that required CMB realignment.

3.2.2. Varying the ULVZ Characteristics

To further assess how ULVZ parameter trade-offs may influence the results obtained with our DAS, the analysis and synthetic modeling were repeated, assuming a range of different δV_P, δV_S, and $\delta\rho$ values. Specifically, δV_P was varied from -5% to -15% in -5% increments, with the δV_S set to create both 1:1 and 1:3 δV_P:δV_S models. These model sets are included to represent both compositionally distinct ULVZs (δV_P:δV_S = 1:1; e.g., Brown et al., 2015; Krier et al., 2021; Thorne & Garnero, 2004) as well as those associated with partial melt in the lowermost mantle (δV_P:δV_S = 1:3; e.g., Berryman, 2000; Rost et al., 2006; Thorne & Garnero, 2004; Williams & Garnero, 1996). $\delta\rho$ values of $+10\%$ and 0% were also both included to represent ULVZs that are/are not intrinsically denser than the surrounding mantle, and the ULVZ thickness was again varied from 0 to 50 km with an increment of 2 km. With this range of characteristics, 301 different synthetic models were evaluated. Six bins that showed robust ULVZ evidence (Section 3.1) were selected as test bins, and the DAS and synthetic modeling were again performed on these bins but now with the other ULVZ models employed to assess how changes to the ULVZ parameters affected our results.

The DAS results do not vary with different values of δV_S and $\delta\rho$; the PcP and PdP travel-times only depend on changes to δV_P. However, the best-fit synthetics for each tested ULVZ model do depend on δV_S and $\delta\rho$ (as well as δV_P) since the PdP amplitude is influenced by each of these parameters (Figure 8; Figures S11 and S12 in Supporting Information S1). When no tomographic corrections were applied, the ULVZ thickness uncertainty (i.e., standard deviation) averaged about 7 km across all the test bins. Somewhat smaller average uncertainties (about 6 km) were obtained when the GLAD-M25 and the SPiRAL tomographic timing corrections were applied (Figures S11 and S12 in Supporting Information S1). Again, since Earth's true velocity structure is not exactly known and since none of the tomographic timing approaches (i.e., no tomographic corrections, corrections using GLAD-M25, corrections using SPiRAL) outperformed the others (Section 3.2.1), we estimate that thickness versus velocity trade-offs result in an approximate 6.5 km uncertainty in our reported ULVZ thicknesses.

Collectively considering the uncertainties from the tomographic timing corrections and the ULVZ parameter trade-offs, our robust ULVZ thicknesses are likely constrained within $\pm$11.5 km. Even with these uncertainties taken into account, our results indicate extensive ULVZ structure across the study region with lateral variations in thickness (Figure 6; Tables S2–S4 in Supporting Information S1).

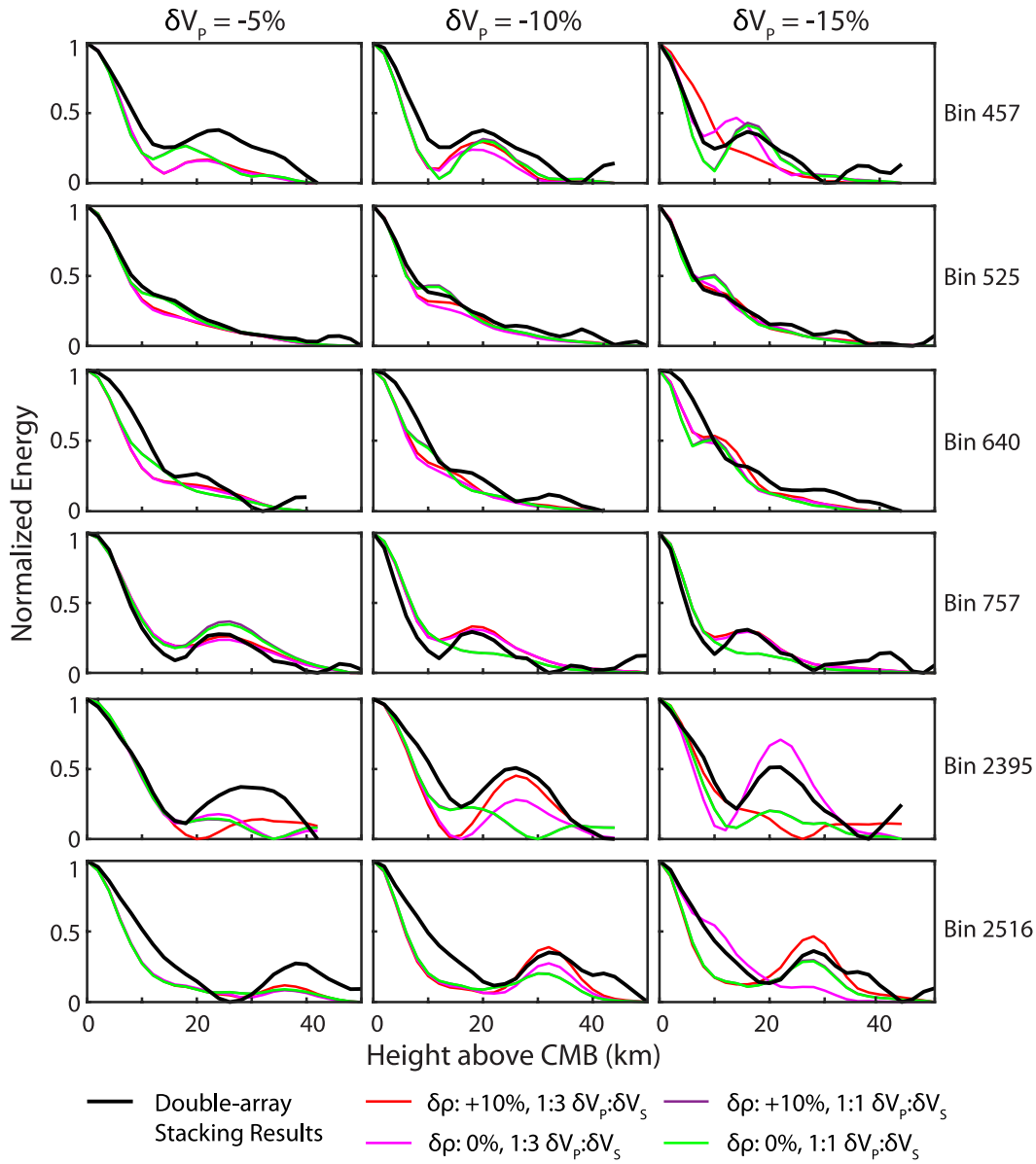

Figure 8. Double-array stacking uncertainty from different ULVZ parameters. The black line in each panel shows the DAS results for one of the six robust test bins (Section 3.2.2) obtained without tomographic timing corrections applied to the data. Colored lines show the best-fit synthetics (i.e., best-fit ULVZ thickness) determined with other assumed ULVZ parameters. Each row corresponds to a different test bin, and each column corresponds to a specific δV_P value (−5%, −10%, or −15%). The δVs and δρ values vary by panel (see legend).

3.2.3. Differentiating ULVZs and UHVZs

As discussed in Section 2.5, our DAS results are based on enveloped PcP waveforms. The polarity normalization from this processing step could potentially make it difficult to differentiate between a PdP reflection generated at the top of a ULVZ versus a reflection from a UHVZ. Therefore, two different tests have been performed to ensure our interpreted signals are associated with ULVZ structure in the lowermost mantle. First, we repeated the DAS analysis for a selection of bins with either robust or ULVZ+ results; however, in this case, we did not envelope the PcP waveforms prior to stacking. As shown in Figure S13 in Supporting Information S1, the non-enveloped results are noisier than those obtained with the method described in Section 2.5, but a PdP-related signal is

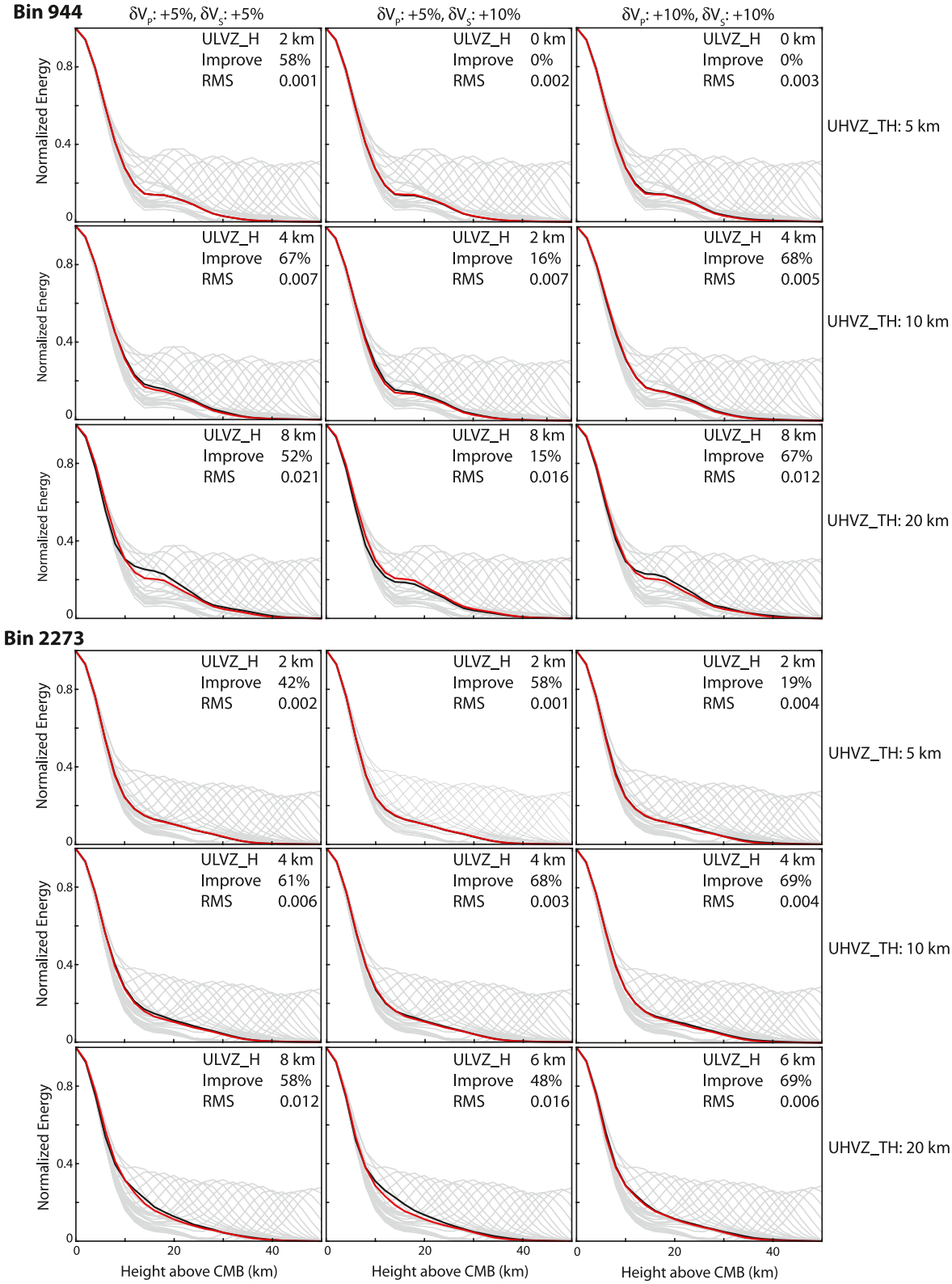

Figure 9.

still observed at the same position above the CMB. This emphasizes the robustness of our findings and illustrates that the PdP signals are not associated with an opposite polarity UHVZ reflection.

Second, we created synthetic PcP waveforms for several UHVZ models to assess if this structure could be mistaken for a ULVZ with our processing approach. Unlike ULVZs, the seismic characteristics of UHVZs have not been extensively investigated. Studies that have examined UHVZs have used S-wave phases (e.g., Yu et al., 2018; Garnero et al., 2020; Pachhai et al., 2022b) and have estimated that the corresponding V_S is ∼10% higher than PREM. That said, these investigations provide no constraints on the potential V_P increase within UHVZs. Given this, both δV_S and δV_P were varied from +5% to +10% in +5% increments in our UHVZ models, but similar to Pachhai et al. (2022b), we did not let δV_P exceed δV_S. UHVZ density variations and thicknesses are largely unconstrained; therefore, we set $\delta\rho = 0\%$, and we used thicknesses of 5, 10, and 20 km. To mimic the analysis performed with the actual data, the synthetic PcP waveforms generated with each UHVZ model were processed using the same DAS procedure described in Section 2.5, and the corresponding output was then modeled using the same suite of ULVZ synthetics described in Section 3.1. Examples of this assessment are shown in Figure 9. As illustrated, the best-fit ULVZ thickness in each case is significantly less than the corresponding UHVZ thickness. The increased velocity within the UHVZ leads to an earlier PcP arrival, which in turn, causes the PcP-PdP time to be reduced. Consequently, the UHVZ DAS results are similar to those for a thin ULVZ. In other words, it is possible to mistakenly interpret UHVZ structure for a ULVZ, but this is only a potential issue for thin (<∼10 km) ULVZ modeling results, which corresponds to less than 8% of our robust bins. Further, given the other possible sources of uncertainty discussed in Sections 3.2.1 and 3.2.2, possible UHVZ misinterpretation has little influence on our results. Our primary conclusion remains unchanged: laterally variable ULVZ structure exists across the southern hemisphere.

4. Discussion: Possible ULVZ Origins

Our findings are in good agreement with existing ULVZ studies in the southern hemisphere. For example, as part of their global study, Thorne and Garnero (2004) found possible, but uncertain, ULVZ structure south of New Zealand, where the current study finds robust ULVZ evidence (Figure 6). Hansen et al. (2020) also found ULVZ evidence in the vicinity of New Zealand as well as beneath the Weddell Sea, and our study also suggests ULVZ structure in these areas. Using PcP waves recorded by the TAMNNET array (Figure 2; Hansen et al., 2015), a 15-station subset of the 238 stations used in the current study, Hansen et al. (2023) found widespread ULVZ evidence beneath the southern hemisphere in some of the same regions where the current study also identifies ULVZs (Figure 10). Both Hansen et al. (2023) and the current study indicate laterally variable ULVZ thickness, thereby providing further confidence in our robust results. Figure S14 in Supporting Information S1 shows a comparison between our results and those of Hansen et al. (2023) for several geographic regions and illustrates the agreement between these two studies.

Our study region is located within a presumed cooler portion of the lowermost mantle, away from the LLVPs (Figure 10); therefore, a compositional origin may better explain our robust ULVZ observations, as opposed to a thermal-only origin. As mentioned in Section 1, compositionally distinct ULVZs may result from iron-enrichment above the CMB, which could be caused by chemical reactions between the silicate mantle and the iron outer core (Kim et al., 2020; Knittle & Jeanloz, 1989; Liu et al., 2023; Ma et al., 2019; Mao et al., 2005, 2006; Nomura et al., 2011; Otsuka & Karato, 2012; Tanaka et al., 2020). That said, the production rate of deep mantle iron-enrichment processes is unclear, and it is uncertain whether such processes would generate sufficient ULVZ materials to explain the widespread distribution observed in our results. Alternatively, compositionally distinct ULVZs may be associated with fractional crystallization of an ancient BMO (Section 1; Boukare et al., 2015; Labrosse et al., 2007). The remaining melt could be enriched in iron, thereby leading to BMO remnants that may have a higher intrinsic density and a lower viscosity compared to the surrounding mantle. However, if ULVZs outside LLVPs are associated with BMO materials, a mechanism is needed to keep the BMO from being

Figure 9. Synthetic DAS results for different UHVZ models. Results are based on the event-station records in robust Bins 944 and 2273. For each bin, the rows correspond to different UHVZ thicknesses (UHVZ_TH), and the columns correspond to different UHVZ δV_P and δV_S values, as labeled. Black lines in each panel show the computed double-array stack, while red and gray lines denote synthetic DAS results for each tested ULVZ thickness. The red line highlights the best-fit synthetic (based on RMS error) to the UHVZ-based DAS result. The best-fit ULVZ thickness (ULVZ_H), the percent improvement in fit compared to PREM (Improve), and the best-fit RMS error (RMS) are also listed.

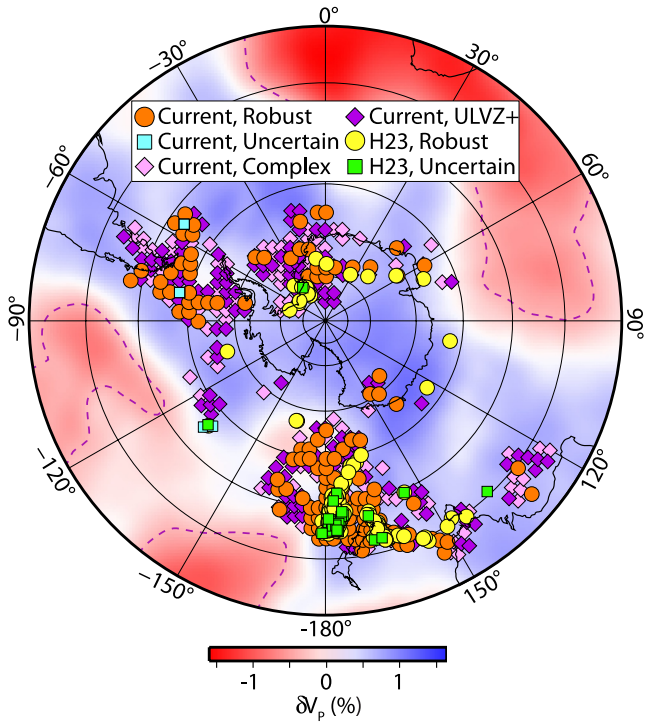

Figure 10. Comparison of results with Hansen et al. (2023). Circles and squares indicate bins showing "robust" and "uncertain" ULVZ evidence, respectively, in each study. Orange and cyan symbols are from the current study, while yellow and green symbols are from Hansen et al. (2023; H23). Pink and purple diamonds indicate bins from the current study classified as "complex" and "ULVZ+," respectively. Background is the GLAD-M25 P-wave tomography model (Lei et al., 2020) at 2800 km depth, with LLVP boundaries denoted by dashed purple lines. The study region is associated with a seismically fast, presumably cool, portion of the lowermost mantle.

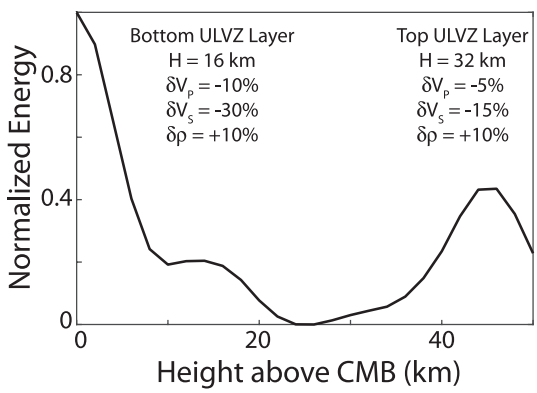

Figure 11. Synthetic DAS results from an example two-layer ULVZ model. Event-station records and corresponding weights from a robust bin (Bin 2281) were used to generate synthetic PcP waveforms for a two-layer ULVZ model, with the thicknesses and parameters indicated in the panel. These synthetic waveforms were then processed with the same DAS technique described in Section 2.5 (assuming a single-layer ULVZ with $\delta V_P = -10\%$, $\delta V_S = -30\%$, and $\delta\rho = +10\%$). The first peak well-matches the thickness of the layer closest to the CMB; however, the slower V_P and V_S of the assumed structure compared to that in the top layer causes the second peak to shift to a shallower mantle depth than that specified in the input model.

completely advected into the LLVP regions after billions of years of mantle convection (Li et al., 2017; McNamara et al., 2010).

Subducted oceanic crust introduced into the lowermost mantle may instead provide a compositionally unique source for our robust ULVZ observations (e.g., Andrault et al., 2014; Dobson & Brodholt, 2005; Hansen et al., 2023; Hirose et al., 1999, 2005; Ma et al., 2016, 2019; Su et al., 2024; Wolf et al., 2024). Mantle convection simulations presented by Hansen et al. (2023), for example, demonstrated how subducted materials can be globally distributed throughout the lowermost mantle with variable concentrations. Subducted mid-ocean ridge basalt (MORB) is intrinsically denser than the background mantle (e.g., Hirose et al., 2005), and numerous studies have indicated that this material could segregate and accumulate on the CMB (e.g., Brandenburg & van Keken, 2007; Christensen & Hofmann, 1994; Jones et al., 2020; Li, 2021, 2023; Mulyukova et al., 2015; Tackley, 2011). However, the seismic characteristics of MORB in the deep mantle remain controversial. Deschamps et al. (2012) and Wang et al. (2020), for example, indicate that subducted oceanic crust would remain seismically fast, even under lowermost mantle temperature and pressure conditions, and as such, would not be compatible with ULVZs. Thomson et al. (2019), on the other hand, suggested that phase transitions associated with $CaSiO_3$ perovskite within subducted MORB could reduce the shear modulus, resulting in seismically slow MORB assemblages in the deep mantle. However, it is uncertain whether this process would lead to seismic velocity reductions as low as those typically estimated for ULVZs. Jones et al. (2020) also argued that subducted oceanic crust could be associated with seismically slow lower mantle anomalies. They suggest that MORB accumulations along the CMB, stabilized by their excess density, would be hotter than the surrounding mantle, leading to reduced seismic velocity.

Our ULVZ+ and complex bins, which we were unable to model with our 1-D synthetics (Section 3.1), may provide further insight on possible ULVZ origins. Extensive 3-D modeling would be needed to fully evaluate the broad range of possible ULVZ parameters and configurations throughout the southern hemisphere, which is not computationally feasible at the present time (Jenkins et al., 2021). That said, the differences in ULVZ thickness indicated by our robust bins suggest lateral ULVZ variability across the CMB. The fact that many of the ULVZ+ and complex bins are interspersed with the robust bins (Figures 6 and 10) may also suggest complicated, internal ULVZ structure (e.g., Pachhai et al., 2023). For example, the two distinct peaks displayed in our ULVZ+ bins may be reflections from a two-layered ULVZ anomaly. Figure 11 shows synthetic DAS results based on an example two-layer ULVZ model, and these are similar to some of our results shown in Figure 5. Complex bins could suggest further heterogeneity, such as additional layering or a gradational velocity structure inside the ULVZs (e.g., Thybo et al., 2003; Idehara, 2011; Pachhai et al., 2015, 2022a; Ross et al., 2004; Rost et al., 2006; Hernlund & Jellinek, 2010), though we cannot rule out the possibility of other anomalous material in the lowermost mantle.

Some prior studies have suggested that layered or gradational velocities within ULVZs could be associated with localized partial melt. Pachhai et al. (2015), for example, examined the lowermost mantle beneath the Tasman Sea, and they suggested that their imaged ULVZ displays a decrease in seismic velocities with depth. They attribute this variable structure to partially molten iron-enriched material with a higher melt fraction closer to the CMB. Thybo et al. (2003) advocated for a similar two-layer ULVZ

structure beneath Siberia, with a dense, melt-rich layer at its base. Rost et al. (2006), on the other hand, suggested that the ULVZ they imaged east of Australia is best modeled by an increase in seismic velocity with depth. They attributed this positive velocity gradient to a change in the melt texture, with pockets of melt closer to the CMB. Hernlund and Jellinek (2010) similarly advocated for positive velocity gradients within ULVZs, caused by dense melt that remains suspended above the CMB due to mantle stirring. Localized partial melting could result from phase transitions of certain lower mantle minerals. For example, Hirose (2006) suggested partial melt along the CMB could result from latent heat released by the exothermic change from perovskite to post-perovskite, which could destabilize the thermal boundary layer at the base of the mantle. However, this phase transition typically occurs 200–300 km above the CMB (e.g., Hirose et al., 2006; Murakami et al., 2004; Ono et al., 2005), and Tackley et al. (2007) indicate it only provides a slight temperature increase. Partial melt could instead be generated by viscous heating in the lowermost mantle (Steinbach & Yuen, 1999), though it has been questioned if such viscous forces could generate sufficient partial melt to explain seismic observations (Dannberg et al., 2021).

Alternatively, it has been consistently shown that subducted oceanic crust has a solidus melting temperature that is ∼250 K lower than the expected CMB temperature conditions (∼4000 K; e.g., Andrault et al., 2014; Hirose et al., 1999; Pradhan et al., 2015). Hydrated, subducted oceanic sediments and lithosphere could also lower solidus melting temperatures (Litasov & Ohtani, 2005). Further, Li (2020) suggested that subducting slabs may promote the formation of hot, ridge-like thermal anomalies near the CMB, which could also lead to localized partial melting, even in relatively cool portions of the lowermost mantle. Partially molten subducted MORB, which would have significantly reduced seismic velocities (e.g., Williams & Garnero, 1996) and increased density (e.g., Hirose et al., 2005) compared to the surrounding lowermost mantle, could be advected by convective flow, moving it away from regions of mantle downwelling (i.e., subduction zones) and toward those of mantle upwelling (i.e., LLVPs; Hernlund & Bonati, 2019; Hansen et al., 2023; Li, 2021, 2023). Accumulations of subducted oceanic crust with different sizes and shapes, as well as different degrees of partial melting, could explain the range of ULVZ thicknesses observed in our robust results as well as the 3-D structure inferred from our ULVZ+ and complex bins. Since our study region is positioned between subduction zones and the LLVPs (Section 1), the ULVZs we have identified may be migrating across the CMB.

5. Conclusions

By analyzing PcP waveforms recorded by stations across Antarctica, our study has significantly expanded ULVZ investigations beneath the southern hemisphere. Also, from a global perspective, the examined, modeled bins have added ∼3.5% new CMB coverage compared to prior ULVZ investigations (Yu & Garnero, 2018). Our DAS results suggest widespread, variable ULVZ structure that, in some locations, can be robustly modeled by 1-D synthetics. However, other portions of the study region show evidence for complicated structure, which may reflect layered or gradational ULVZs. Our findings are consistent with those of Hansen et al. (2023), who suggested that ULVZs can be predominantly explained by variable accumulations of subducted oceanic crust with partial melting in the lowermost mantle.

Data Availability Statement

The facilities of SAGE Data Services, particularly the SAGE Data Management Center, were used to access the waveforms and related metadata used in this project (http://ds.iris.edu/mda/). Specifically, the following data sets were employed in our analysis: Alfred Wegener Institute for Polar and Marine Research (1993); Anandakrishnan (1997); Anandakrishnan et al. (2000); ASL/USGS (1993, 2014); Aster and Kyle (1996, 1999, 2007); Bascou and Barruol (2015); Brisbourne et al. (2016); GEOFON Data Centre (1993); Hansen (2012); Herbert and Data Group (2016); Holland and Bindschadler (2012); IPGP and EOST (1982); Istituto Nazionale di Oceanografia e di Geofisica Sperimentale (1992); MedNet Project Partner Institutions (1990); Okal and Macayeal (2003); Parker and Beaudoin (2007); Wiens (1997); Wiens et al. (2007, 2014); Wiens and Nyblade (2007). Further details are provided in Table S1 in Supporting Information S1. SAGE Data Services are funded through the Seismological Facilities for the Advancement of Geoscience (SAGE) Award of the National Science Foundation under Cooperative Support Agreement EAR-1851048. Some figures were generated with the Generic Mapping Tools software (Wessel et al., 2013).

Acknowledgments
We thank two anonymous reviewers for their thorough critiques of our manuscript. Funding for this research was provided by the National Science Foundation (Grants PLR-1643551, EAR-1855624, and EAR-2216564) and by the Natural Environment Research Council (Grants NE/R012199/1 and NE/W005247/1).

References

Albuquerque Seismological Laboratory (ASL)/USGS. (1993). Global telemetered seismograph network (USAF/USGS) [Dataset]. *International Federation of Digital Seismograph Networks*. https://doi.org/10.7914/SN/GT

Albuquerque Seismological Laboratory (ASL)/USGS. (2014). Global seismograph network (GSN – IRIS/USGS) [Dataset]. *International Federation of Digital Seismograph Networks*. https://doi.org/10.7914/SN/IU

Alfred Wegener Institute for Polar and Marine Research. (1993). AWI network Antarctica [Dataset]. *GFZ Data Services*. https://doi.org/10.14470/NJ617293

Ammon, C. J. (1991). The isolation of receiver effects from teleseismic P waveforms. *Bulletin of the Seismological Society of America*, *81*(6), 2504–2510. https://doi.org/10.1785/bssa0810062504

Anandakrishnan, S. (1997). Antarctic network of unattended broadband seismometers [Dataset]. *International Federation of Digital Seismograph Networks*. https://doi.org/10.7914/SN/YI_1997

Anandakrishnan, S., Wiens, D., & Nyblade, A. (2000). A broadband seismic investigation of deep continental structure across the east-west Antarctic boundary [Dataset]. *International Federation of Digital Seismograph Networks*. https://doi.org/10.7914/SN/XP_2000

Andrault, D., Pesce, G., Bouhifd, M. A., Bolfan-Casanova, N., Hénot, J. M., & Mezouar, M. (2014). Melting of subducted basalt at the core-mantle boundary. *Science*, *344*(6186), 892–895. https://doi.org/10.1126/science.1250466

Aster, R., & Kyle, P. (1996). Mount Erebus observatory [Dataset]. *International Federation of Digital Seismograph Networks*. https://doi.org/10.7914/SN/XS_1996

Aster, R., & Kyle, P. (1999). Mount Erebus seismic studies [Dataset]. *International Federation of Digital Seismograph Networks*. https://doi.org/10.7914/SN/XZ_1999

Aster, R., & Kyle, P. (2007). Erebus tomography and source studies [Dataset]. *International Federation of Digital Seismograph Networks*. https://doi.org/10.7914/SN/ZW_2007

Avants, M., Lay, T., & Garnero, E. J. (2006). A new probe of ULVZ S-wave velocity structure: Array stacking of ScS waveforms. *Geophysical Research Letters*, *33*(7), L07314. https://doi.org/10.1029/2005GL024989

Bascou, J., & Barruol, G. (2015). ArLiTA: Architecture de la Lithosphère de Terre Adélie, Antarctique [Dataset]. *RESIF – Réseau Sismologique et géodésique Français*. https://doi.org/10.15778/resif.1a2009

Berryman, J. G. (2000). Seismic velocity decrement ratios for regions of partial melt in the lower mantle. *Geophysical Research Letters*, *27*(3), 421–424. https://doi.org/10.1029/1999gl008402

Boukare, C. E., Ricard, Y., & Fiquet, G. (2015). Thermodynamics of the MgO-FeO-SiO2 system up to 140 GPa: Application to the crystallization of Earth's magma ocean. *Journal of Geophysical Research: Solid Earth*, *120*(9), 6085–6101. https://doi.org/10.1002/2015jb011929

Bower, D. J., Wicks, J. K., Gurnis, M., & Jackson, J. M. (2011). A geodynamic and mineral physics model of a solid-state ultralow-velocity zone. *Earth and Planetary Science Letters*, *303*(3–4), 193–202. https://doi.org/10.1016/j.epsl.2010.12.035

Brandenburg, J. P., & van Keken, P. E. (2007). Methods for thermochemical convection in Earth's mantle with force-balanced plates. *Geochemistry, Geophysics, Geosystems*, *8*(11), Q11004. https://doi.org/10.1029/2007GC001692

Brisbourne, A., Stuart, G., & O'Donnell, J. P. (2016). UKANET: UK Antarctic network [Dataset]. *International Federation of Digital Seismography Networks*. https://doi.org/10.7914/SN/1D_2016

Brown, S. P., Thorne, M. S., Miyagi, L., & Rost, S. (2015). A compositional origin to ultralow-velocity zones. *Geophysical Research Letters*, *42*(4), 1039–1045. https://doi.org/10.1002/2014gl062097

Cameron, B. I., Walker, J. A., Carr, M. J., Patino, L. C., Matıas, O., & Feigenson, M. D. (2003). Flux versus decompression melting at stratovolcanoes in southeastern Guatemala. *Journal of Volcanology and Geothermal Research*, *119*(1–4), 21–50. https://doi.org/10.1016/s0377-0273(02)00304-9

Christensen, U. R., & Hofmann, A. W. (1994). Segregation of subducted oceanic crust in the convecting mantle. *Journal of Geophysical Research*, *99*(B10), 19867–19884. https://doi.org/10.1029/93jb03403

Cottaar, S., & Romanowicz, B. (2012). An unusually large ULVZ at the base of the mantle near Hawaii. *Earth and Planetary Science Letters*, *355*, 213–222. https://doi.org/10.1016/j.epsl.2012.09.005

Crotwell, H. P., Owen, T. J., & Ritsema, J. (1999). The TauP toolkit: Flexible seismic travel-time and ray-path utilities. *Seismological Research Letters*, *70*(2), 154–160. https://doi.org/10.1785/gssrl.70.2.154

Dannberg, J., Myhill, R., Gassmoller, R., & Cottaar, S. (2021). The morphology, evolution and seismic visibility of partial melt at the core-mantle boundary: Implications for ULVZs. *Geophysical Journal International*, *227*(2), 1028–1059. https://doi.org/10.1093/gji/ggab242

Deschamps, F., Cobden, L., & Tackley, P. J. (2012). The primitive nature of large low shear-wave velocity provinces. *Earth and Planetary Science Letters*, *349*, 198–208. https://doi.org/10.1016/j.epsl.2012.07.012

Dobson, D. P., & Brodholt, J. P. (2005). Subducted banded iron formations as a source of ultralow-velocity zones at the core–mantle boundary. *Nature*, *434*(7031), 371–374. https://doi.org/10.1038/nature03430

Dziewonski, A. M., & Anderson, D. L. (1981). Preliminary reference Earth model. *Physics of the Earth and Planetary Interiors*, *25*(4), 297–356. https://doi.org/10.1016/0031-9201(81)90046-7

Dziewonski, A. M., Chou, T.-A., & Woodhouse, J. H. (1981). Determination of earthquake source parameters from waveform data for studies of global and regional seismicity. *Journal of Geophysical Research*, *86*(B4), 2825–2852. https://doi.org/10.1029/jb086ib04p02825

Dziewonski, A. M., Hager, B. H., & O'Connell, R. J. (1977). Large-scale heterogeneities in the lower mantle. *Journal of Geophysical Research*, *82*(2), 239–255. https://doi.org/10.1029/jb082i002p00239

Ekström, G., Nettles, M., & Dziewonski, A. M. (2012). The global CMT project 2004-2010: Centroid-moment tensors for 13,017 earthquakes. *Physics of the Earth and Planetary Interiors*, *200–201*, 1–9. https://doi.org/10.1016/j.pepi.2012.04.002

Fan, A., & Sun, X. (2021). Origin of ULVZs near the African LLSVP: Implications from their distribution and characteristics. *Earthquake Science*, *34*(4), 299–309. https://doi.org/10.29382/eqs-2021-0042

Forte, A. M., & Mitrovica, J. X. (2001). Deep-mantle high-viscosity flow and thermochemical structure inferred from seismic and geodynamic data. *Nature*, *410*(6832), 1049–1056. https://doi.org/10.1038/35074000

Garnero, E. J. (2000). Heterogeneity of the lowermost mantle. *Annual Review of Earth and Planetary Sciences*, *28*(1), 509–537. https://doi.org/10.1146/annurev.earth.28.1.509

Garnero, E. J., & Helmberger, D. V. (1998). Further structural constraints and uncertainties of a thin laterally varying ultralow-velocity layer at the base of the mantle. *Journal of Geophysical Research*, *103*(B6), 12495–12509. https://doi.org/10.1029/98jb00700

Garnero, E. J., & Jeanloz, R. (2000). Earth's enigmatic interface. *Science*, *289*(5476), 70–71. https://doi.org/10.1126/science.289.5476.70

Garnero, E. J., & McNamara, A. K. (2008). Structure and dynamics of Earth's lower mantle. *Science*, *320*(5876), 626–628. https://doi.org/10.1126/science.1148028

Garnero, E. J., Revenaugh, J., Williams, Q., Lay, T., & Kellogg, L. H. (1998). Ultralow velocity zone at the core-mantle boundary. *The Core-Mantle Boundary Region*, *28*, 319–334. https://doi.org/10.1029/gd028p0319

Garnero, E. J., & Vidale, J. E. (1999). ScP; a probe of ultralow velocity zones at the base of the mantle. *Geophysical Research Letters*, *26*(3), 377–380. https://doi.org/10.1029/1998gl900319

Garnero, E. J., Yu, S., Shim, S. H., Li, M., Ko, B., Thorne, M. S., & Zhao, C. (2020). *Ultra height velocity zones at the core-mantle boundary, abstract DI008-05*. American Geophysical Union.

GEOFON Data Centre. (1993). GEOFON seismic network [Dataset]. *GFZ Data Services*. https://doi.org/10.14470/TR560404

Gilbert, F., & Helmberger, D. V. (1972). Generalized ray theory for a layered sphere. *Geophysical Journal International*, *27*(1), 57–80. https://doi.org/10.1111/j.1365-246x.1972.tb02347.x

Hansen, S. (2012). Transantarctic Mountains northern network [Dataset]. *International Federation of Digital Seismograph Networks*. https://doi.org/10.7914/SN/ZJ_2012

Hansen, S. E., Carson, S. E., Garnero, E. J., Rost, S., & Yu, S. (2020). Investigating ultra-low velocity zones in the southern hemisphere using an Antarctic dataset. *Earth and Planetary Science Letters*, *536*, 116142. https://doi.org/10.1016/j.epsl.2020.116142

Hansen, S. E., Garnero, E. J., Li, M., Shim, S.-H., & Rost, S. (2023). Globally distributed subducted materials along the Earth's core-mantle boundary: Implications for ultralow velocity zones. *Science Advances*, *9*(14). https://doi.org/10.1126/sciadv.add4838

Hansen, S. E., Garnero, E. J., & Rost, S. (2021). Historical interstation pattern referencing (HIPR): An application to PcP waves recorded in the Antarctic for ULVZ imaging. *Journal of Geophysical Research: Solid Earth*, *126*(10), e2021JB022741. https://doi.org/10.1029/2021JB022741

Hansen, S. E., Reusch, A. M., Parker, T., Bloomquist, D. K., Carpenter, P., Graw, J. H., & Brenn, G. R. (2015). The transantarctic mountains northern network (TAMNNET): Deployment and performance of a seismic array in Antarctica. *Seismological Research Letters*, *86*(6), 1636–1644. https://doi.org/10.1785/0220150117

Havens, E., & Revenaugh, J. (2001). A broadband seismic study of the lowermost mantle beneath Mexico: Constraints on ultralow velocity zone elasticity and density. *Journal of Geophysical Research*, *106*(B12), 30809–30820. https://doi.org/10.1029/2000jb000072

Herbert, J., & Data Group. (2016). Interim broadband monitoring of the Mount Erebus volcano [Dataset]. *International Federation of Digital Seismograph Networks*. https://doi.org/10.7914/SN/2H_2016

Hernlund, J., McNamara, A., & Schubert, G. (2015). 7.11: The core–mantle boundary region. *Treatise on Geophysics*, *2*(7), 461–519.

Hernlund, J. W., & Bonati, I. (2019). Modeling ultralow velocity zones as a thin chemically distinct dense layer at the core-mantle boundary. *Journal of Geophysical Research: Solid Earth*, *124*(8), 7902–7917. https://doi.org/10.1029/2018jb017218

Hernlund, J. W., & Jellinek, A. M. (2010). Dynamics and structure of a stirred partially molten ultralow-velocity zone. *Earth and Planetary Science Letters*, *296*(1–2), 1–8. https://doi.org/10.1016/j.epsl.2010.04.027

Hirose, K. (2006). Postperovskite phase transition and its geophysical implications. *Reviews of Geophysics*, *44*(3), RG3001. https://doi.org/10.1029/2005RG000186

Hirose, K., Fei, Y., Ma, Y., & Mao, H. (1999). The fate of subducted basaltic crust in the Earth's lower mantle. *Nature*, *397*(6714), 53–56. https://doi.org/10.1038/16225

Hirose, K., Sinmo, R., Sata, N., & Ohishi, Y. (2006). Determination of post-perovskite phase transition boundary in MgSiO3 using Au and MgO pressure standards. *Geophysical Research Letters*, *33*(1), L01310. https://doi.org/10.1029/2005GL024468

Hirose, K., Takafuji, N., Sata, N., & Ohishi, Y. (2005). Phase transition and density of subducted MORB crust in the lower mantle. *Earth and Planetary Science Letters*, *237*(1–2), 239–251. https://doi.org/10.1016/j.epsl.2005.06.035

Holland, D., & Bindschadler, R. (2012). Observing Pine Island Glacier (PIG) ice shelf deformation and fracture using a GPS and Seismic Network [Dataset]. *International Federation of Digital Seismograph Networks*. https://doi.org/10.7914/SN/XC_2012

Hutko, A. R., Lay, T., & Revenaugh, J. (2009). Localized double-array stacking analysis of PcP: D″ and ULVZ structure beneath the Cocos plate, Mexico, central Pacific, and north Pacific. *Physics of the Earth and Planetary Interiors*, *173*(1–2), 60–74. https://doi.org/10.1016/j.pepi.2008.11.003

Idehara, K. (2011). Structural heterogeneity of an ultra-low-velocity zone beneath the Philippine Islands: Implications for core–mantle chemical interactions induced by massive partial melting at the bottom of the mantle. *Physics of the Earth and Planetary Interiors*, *184*(1–2), 80–90. https://doi.org/10.1016/j.pepi.2010.10.014

Institut de physique du globe de Paris (IPGP) and Ecole et Observatoire des Sciences de la Terre de Strasbourg (EOST). (1982). GEOSCOPE, French global network of broadband seismic stations [Dataset]. *IPGP, Université de Paris*. https://doi.org/10.18715/GEOSCOPE.G

Istituto Nazionale di Oceanografia e di Geofisica Sperimentale. (1992). Antarctic seismographic argentinean Italian network – ASAIN [Dataset]. *International Federation of Digital Seismograph Networks*. https://doi.org/10.7914/SN/AI

Jenkins, J., Mousavi, S., Li, Z., & Cottaar, S. (2021). A high-resolution map of Hawaiian ULVZ morphology from ScS phases. *Earth and Planetary Science Letters*, *563*(1), 116885. https://doi.org/10.1016/j.epsl.2021.116885

Jensen, K. J., Thorne, M. S., & Rost, S. (2013). SPdKS analysis of ultralow-velocity zones beneath the western Pacific. *Geophysical Research Letters*, *40*(17), 4574–4578. https://doi.org/10.1002/grl.50877

Jones, T. D., Maguire, R. R., van Keken, P. E., Ritsema, J., & Koelemeijer, P. (2020). Subducted oceanic crust as the origin of seismically slow lower-mantle structures. *Progress in Earth and Planetary Science*, *7*(17), 17. https://doi.org/10.1186/s40645-020-00327-1

Kim, T., Ko, B., Greenberg, E., Prakapenka, V., Shim, S.-H., & Lee, Y. (2020). Low melting temperature of anhydrous mantle materials at the core-mantle boundary. *Geophysical Research Letters*, *47*(20), e2020GL089345. https://doi.org/10.1029/2020GL089345

Knittle, E., & Jeanloz, R. (1989). Simulating the core-mantle boundary: An experimental study of high-pressure reactions between silicates and liquid iron. *Geophysical Research Letters*, *16*(7), 609–612. https://doi.org/10.1029/gl016i007p00609

Knittle, E., & Jeanloz, R. (1991). Earth's core-mantle boundary: Results of experiments at high pressures and temperatures. *Science*, *251*(5000), 1438–1443. https://doi.org/10.1126/science.251.5000.1438

Krier, J., Thorne, M. S., Leng, K., & Nissen-Meyer, T. (2021). A compositional component to the Samoa ultralow-velocity zone revealed through 2- and 3-D waveform modeling of SKS and SKKS differential travel-times and amplitudes. *Journal of Geophysical Research: Solid Earth*, *126*(7), e2021JB021897. https://doi.org/10.1029/2021JB021897

Krüger, F., Weber, M., Scherbaum, F., & Schlittenhardt, J. (1993). Double beam analysis of anomalies in the core-mantle boundary region. *Geophysical Research Letters*, *20*(14), 1475–1478. https://doi.org/10.1029/93gl01311

Labrosse, S., Hernlund, J. W., & Coltice, N. (2007). A crystallizing dense magma ocean at the base of the Earth's mantle. *Nature*, *450*(7171), 866–869. https://doi.org/10.1038/nature06355

Lai, V. H., Helmberger, D. V., Dobrosavljevic, V. V., Wu, W., Sun, D., Jackson, J. M., & Gurnis, M. (2022). Strong ULVZ and slab interaction at the northeastern edge of the Pacific LLSVP favors plume generation. *Geochemistry, Geophysics, Geosystems*, *23*(2), e2021GC010020. https://doi.org/10.1029/2021GC010020

Langston, C. A. (1979). Structure under Mount Rainier, Washington, inferred from teleseismic body waves. *Journal of Geophysical Research*, *84*(B9), 4749–4762. https://doi.org/10.1029/jb084ib09p04749

Lay, T. (1989). Structure of the core-mantle transition zone. *Eos, Transactions American Geophysical Union*, *70*(4), 49–59. https://doi.org/10.1029/89eo00024

Lay, T., Hernlund, J., & Buffett, B. A. (2008). Core–mantle boundary heat flow. *Nature Geoscience*, *1*(1), 25–32. https://doi.org/10.1038/ngeo.2007.44

Lei, W., Ruan, Y., Bozdağ, E., Peter, D., Lefebvre, M., Komatitsch, D., et al. (2020). Global adjoint tomography—Model GLAD- M25. *Geophysical Journal International*, *223*(1), 1–21. https://doi.org/10.1093/gji/ggaa253

Li, J., Sun, D., & Bower, D. J. (2022). Slab control on the mega-sized North Pacific ultra-low velocity zone. *Nature Communications*, *13*(1042), 1042. https://doi.org/10.1038/s41467-022-28708-8

Li, M. (2020). The formation of hot thermal anomalies in cold subduction-influenced regions of Earth's lowermost mantle. *Journal of Geophysical Research: Solid Earth*, *125*(6), e2019JB019312. https://doi.org/10.1029/2019JB019312

Li, M. (2021). The cycling of subducted oceanic crust in the Earth's deep mantle. In *Mantle convection and surface expressions* (pp. 303–328).

Li, M. (2023). Variable distribution of subducted oceanic crust beneath subduction regions of the lowermost mantle. *Physics of the Earth and Planetary Interiors*, *341*, 107063. https://doi.org/10.1016/j.pepi.2023.107063

Li, M., McNamara, A. K., Garnero, E. J., & Yu, S. (2017). Compositionally-distinct ultra-low velocity zones on Earth's core-mantle boundary. *Nature Communications*, *8*(177), 177. https://doi.org/10.1038/s41467-017-00219-x

Li, Z., Leng, K., Jenkins, J., & Cottaar, S. (2022). Kilometer-scale structure on the core-mantle boundary near Hawaii. *Nature Communications*, *13*(2787), 2787. https://doi.org/10.1038/s41467-022-30502-5

Litasov, K. D., & Ohtani, E. (2005). Phase relations in hydrous MORB at 18-28 GPa: Implications for heterogeneity of the lower mantle. *Physics of the Earth and Planetary Interiors*, *150*(4), 239–263. https://doi.org/10.1016/j.pepi.2004.10.010

Liu, H., Liu, L., Xin, C., Yang, L., & Gu, X. (2023). A first-principles study of the structural, electronic, and elastic properties of the FeO2-FeO2He system under high pressure. *Physical Chemistry Chemical Physics*, *30*. https://doi.org/10.1039/D3CP02315J

Loper, D. E., & Lay, T. (1995). The core-mantle boundary region. *Journal of Geophysical Research*, *100*(B4), 6397–6420. https://doi.org/10.1029/94jb02048

Ma, X., Sun, X., & Thomas, C. (2019). Localized ultra-low velocity zones at the eastern boundary of Pacific LLSVP. *Earth and Planetary Science Letters*, *507*, 40–49. https://doi.org/10.1016/j.epsl.2018.11.037

Ma, X., Sun, X., Wiens, D. A., Wen, L., Nyblade, A., Anandakrishnan, S., et al. (2016). Strong seismic scatterers near the core-mantle boundary north of the Pacific anomaly. *Physics of the Earth and Planetary Interiors*, *253*, 21–30. https://doi.org/10.1016/j.pepi.2016.01.007

Mao, W. L., Mao, H., Sturhahn, W., Zhao, J., Prakapenka, V. B., Meng, Y., et al. (2006). Iron-rich post-perovskite and the origin of ultralow-velocity zones. *Science*, *312*(5773), 564–565. https://doi.org/10.1126/science.1123442

Mao, W. L., Meng, Y., Shen, G., Prakapenka, V. B., Campbell, A. J., Heinz, D. L., et al. (2005). Iron-rich silicates in the Earth's D″ layer. *Proceedings of the National Academy of Sciences*, *102*(28), 9751–9753. https://doi.org/10.1073/pnas.0503737102

McNamara, A. K., Garnero, E. J., & Rost, S. (2010). Tracking deep mantle reservoirs with ultra-low velocity zones. *Earth and Planetary Science Letters*, *299*(1–2), 1–9. https://doi.org/10.1016/j.epsl.2010.07.042

MedNet Project Partner Institutions. (1990). Mediterranean very broadband seismographic network (MedNet) [Dataset]. *Istituto Nazionale di Geofisica e Vulcanologia*. https://doi.org/10.13127/SD/FBBBTDTD6Q

Mulyukova, E., Steinberger, B., Dabrowski, M., & Sobolev, S. V. (2015). Survival of LLSVPs for billions of years in a vigorously convecting mantle: Replenishment and destruction of chemical anomaly. *Journal of Geophysical Research: Solid Earth*, *120*(5), 3824–3847. https://doi.org/10.1002/2014jb011688

Murakami, M., Hirose, K., Kawamura, K., Sata, N., & Ohishi, Y. (2004). Post-perovskite phase transition in MgSiO3. *Science*, *304*(5672), 855–858. https://doi.org/10.1126/science.1095932

Nomura, R., Hirose, K., Uesugi, K., Ohishi, Y., Tsuchiyama, A., Miyake, A., & Ueno, Y. (2014). Low core-mantle boundary temperature inferred from the solidus of pyrolite. *Science*, *343*(6170), 522–525. https://doi.org/10.1126/science.1248186

Nomura, R., Ozawa, H., Tateno, S., Hirose, K., Hernlund, J., Muto, S., et al. (2011). Spin crossover and iron-rich silicate melt in the Earth's deep mantle. *Nature*, *473*(7346), 199–202. https://doi.org/10.1038/nature09940

Okal, E., & MacAyeal, D. (2003). Collaborative research of the Earth's largest icebergs [Dataset]. *International Federation of Digital Seismograph Networks*. https://doi.org/10.7914/SN/XV_2003

Ono, S., Oganov, A. R., Koyama, T., & Shimizu, H. (2006). Stability and compressibility of the high-pressure phases of Al2O3 up to 200 GPa: Implications for the electrical conductivity of the base of the lower mantle. *Earth and Planetary Science Letters*, *246*(3–4), 326–335. https://doi.org/10.1016/j.epsl.2006.04.017

Ono, S., Oganov, A. R., & Ohishi, Y. (2005). In situ observations of phase transition between perovskite and CaIrO3-type phase in MgSiO3 and pyrolitic mantle composition. *Earth and Planetary Science Letters*, *236*(3–4), 914–932. https://doi.org/10.1016/j.epsl.2005.06.001

Otsuka, K., & Karato, S. I. (2012). Deep penetration of molten iron into the mantle caused by a morphological instability. *Nature*, *492*(7428), 243–246. https://doi.org/10.1038/nature11663

Pachhai, S., Dettmer, J., & Tkalčić, H. (2015). Ultra-low velocity zones beneath the Philippine and Tasman Seas revealed by a trans-dimensional Bayesian waveform inversion. *Geophysical Journal International*, *203*(2), 1302–1318. https://doi.org/10.1093/gji/ggv368

Pachhai, S., Li, M., Thorne, M. S., Dettmer, J., & Tkalčić, H. (2022a). Internal structure of ultralow velocity zones consistent with origin from a basal magma ocean. *Nature Geoscience*, *15*(1), 79–84. https://doi.org/10.1038/s41561-021-00871-5

Pachhai, S., Thorne, M. S., & Nissen-Meyer, T. (2022b). Quantification of small-scale heterogeneity at the Core-Mantle boundary using sample entropy of SKS and SPdKS synthetic waveforms. *Minerals*, *12*(7), 813. https://doi.org/10.3390/min12070813

Pachhai, S., Thorne, M. S., & Rost, S. (2023). Improved characterization of ultralow-velocity zones through advances in Bayesian inversion of ScP wavesforms. *Journal of Geophysical Research: Solid Earth*, *128*(6), e2023JB026415. https://doi.org/10.1029/2023JB026415

Parker, T., & Beaudoin, B. (2007). Development of a power and communication for remote autonomous GPS and seismic stations in Antarctica [Dataset]. *International Federation of Digital Seismograph Networks*. https://doi.org/10.7914/SN/XD_2007

Persh, S. E., Vidale, J. E., & Earle, P. S. (2001). Absence of short-period ULVZ precursors to PcP and ScP from two regions of the CMB. *Geophysical Research Letters*, *28*(2), 387–390. https://doi.org/10.1029/2000gl011607

Pradhan, G. K., Fiquet, G., Siebert, J., Auzende, A.-L., Morard, G., Antonangeli, D., & Garbarino, G. (2015). Melting of MORB at core-mantle boundary. *Earth and Planetary Science Letters*, *431*, 247–255. https://doi.org/10.1016/j.epsl.2015.09.034

Raddick, M. J., Parmentier, E. M., & Scheirer, D. S. (2002). Buoyant decompression melting: A possible mechanism for intraplate volcanism. *Journal of Geophysical Research*, *107*(B10), ECV7-1–ECV7-14. https://doi.org/10.1029/2001JB000617

Reasoner, C., & Revenaugh, J. (1999). Short-period P wave constraints on D″ reflectivity. *Journal of Geophysical Research*, *104*(B1), 955–961. https://doi.org/10.1029/1998jb900053

Reasoner, C., & Revenaugh, J. (2000). ScP constraints on ultralow-velocity zone density and gradient thickness beneath the Pacific. *Journal of Geophysical Research*, *105*(B12), 28173–28182. https://doi.org/10.1029/2000jb900331

Revenaugh, J., & Meyer, R. (1997). Seismic evidence of partial melt within a possibly ubiquitous low-velocity layer at the base of the mantle. *Science*, *277*(5326), 670–673. https://doi.org/10.1126/science.277.5326.670

Rondenay, S., & Fischer, K. M. (2003). Constraints on localized core-mantle boundary structure from multichannel, broadband SKS coda analysis. *Journal of Geophysical Research*, *108*(B11), 2537. https://doi.org/10.1029/2003JB002518

Ross, A., Thybo, H., & Solidilov, L. (2004). Reflection seismic profiles of the core-mantle boundary. *Journal of Geophysical Research*, *109*(B8), B08303. https://doi.org/10.1029/2003jb002515

Rost, S., Garnero, E. J., Thorne, M. S., & Hutko, A. R. (2010). On the absence of an ultralow-velocity zone in the North Pacific. *Journal of Geophysical Research*, *115*(B4), B04312. https://doi.org/10.1029/2009JB006420

Rost, S., Garnero, E. J., & Williams, Q. (2006). Fine-scale ultralow velocity zone structure from high-frequency seismic array data. *Journal of Geophysical Research*, *111*(B9), B09310. https://doi.org/10.1029/2005JB004088

Rost, S., Garnero, E. J., Williams, Q., & Manga, M. (2005). Seismological constraints on a possible plume root at the core–mantle boundary. *Nature*, *435*(7042), 666–669. https://doi.org/10.1038/nature03620

Shearer, P. M., & Flanagan, M. P. (1999). Seismic velocity and density jumps across the 410-and 660-kilometer discontinuities. *Science*, *285*(5433), 1545–1548. https://doi.org/10.1126/science.285.5433.1545

Simmons, N. A., Myers, S. C., Morency, C., Chiang, A., & Knapp, D. R. (2021). SPiRaL: A multiresolution global tomography model of seismic wave speeds and radial anisotropy variations in the crust and mantle. *Geophysical Journal International*, *227*(2), 1366–1391. https://doi.org/10.1093/gji/ggab277

Steinbach, V., & Yuen, D. A. (1999). Viscous heating: A potential mechanism for the formation of the ultralow velocity zone. *Earth and Planetary Science Letters*, *172*(3–4), 213–220. https://doi.org/10.1016/s0012-821x(99)00205-8

Steinberger, B., & Holme, R. (2008). Mantle flow models with core-mantle boundary constraints and chemical heterogeneities in the lowermost mantle. *Journal of Geophysical Research*, *113*(B5), B05403. https://doi.org/10.1029/2007JB005080

Su, Y., Ni, S., Zhang, B., Chen, Y., Wu, W., Li, M., et al. (2024). Detections of ultralow velocity zones in high-velocity lowermost mantle linked to subducted slabs. *Nature Geoscience*. https://doi.org/10.1038/s41561-024-01394-5

Tackley, P. J. (2011). Living dead slabs in 3-D: The dynamics of compositionally-stratified slabs entering a "slab graveyard" above the core-mantle boundary. *Physics of the Earth and Planetary Interiors*, *188*(3–4), 150–162. https://doi.org/10.1016/j.pepi.2011.04.013

Tackley, P. J., Nakagawa, T., & Hernlund, J. W. (2007). Influence of the post-perovskite transition on thermal and thermo-chemical mantle convection. In *Post-perovskite: The last mantle phase transition*. In *Geophysical monograph series* (Vol. 174, pp. 229–247). https://doi.org/10.1029/174gm16

Tanaka, R., Sakamaki, T., Ohtani, E., Fukui, H., Kamada, S., Suzuki, A., et al. (2020). The sound velocity of wüstite at high pressures: Implications for low-velocity anomalies at the base of the lower mantle. *Progress in Earth and Planetary Science*, *7*(23), 23. https://doi.org/10.1186/s40645-020-00333-3

Thomson, A. R., Crichton, W. A., Brodholt, J. P., Wood, I. G., Siersch, N. C., Muir, J. M. R., et al. (2019). Seismic velocities of CaSiO3 perovskite can explain LLSPVs in Earth's lower mantle. *Nature*, *572*(7771), 643–647. https://doi.org/10.1038/s41586-019-1483-x

Thorne, M. S., & Garnero, E. J. (2004). Inferences on ultralow-velocity zone structure from a global analysis of SPdKS waves. *Journal of Geophysical Research*, *109*(B8), B08301. https://doi.org/10.1029/2004JB003010

Thorne, M. S., Garnero, E. J., Jahnke, G., Igel, H., & McNamara, A. K. (2013). Mega ultra low velocity zone and mantle flow. *Earth and Planetary Science Letters*, *364*, 59–67. https://doi.org/10.1016/j.epsl.2012.12.034

Thorne, M. S., Leng, K., Pachhai, S., Rost, S., Wicks, J., & Nissen-Meyer, T. (2020b). The most parsimonious ultralow-velocity zone distribution from highly anomalous SPdKS waveforms. *Geochemistry, Geophysics, Geosystems*, *22*(1), e2020GC009467. https://doi.org/10.1029/2020GC009467

Thorne, M. S., Pachhai, S., Leng, K., Wicks, J. K., & Nissen-Meyer, T. (2020a). New candidate ultralow-velocity zone locations from highly anomalous SPdKS waveforms. *Minerals*, *10*(211), 211. https://doi.org/10.3390/min10030211

Thybo, H., Ross, A. R., & Egorkin, A. V. (2003). Explosion seismic reflections from the Earth's core. *Earth and Planetary Science Letters*, *216*(4), 693–702. https://doi.org/10.1016/s0012-821x(03)00532-6

Trampert, J., Vacher, P., & Vlaar, N. (2001). Sensitivities of seismic velocities to temperature, pressure and composition in the lower mantle. *Physics of the Earth and Planetary Interiors*, *124*(3–4), 255–267. https://doi.org/10.1016/s0031-9201(01)00201-1

van der Hilst, R. D., De Hoop, M. V., Wang, P., Shim, S. H., Ma, P., & Tenorio, L. (2007). Seismostratigraphy and thermal structure of Earth's core-mantle boundary region. *Science*, *315*(5820), 1813–1817. https://doi.org/10.1126/science.1137867

Wang, W., Xu, Y., Sun, D., Ni, S., Wentzcovitch, R., & Wu, Z. (2020). Velocity and density characteristics of subducted oceanic crust and the origin of lower-mantle heterogeneities. *Nature Communications*, *11*(1), 64. https://doi.org/10.1038/s41467-019-13720-2

Wen, L. (2000). Intense seismic scattering near the Earth's core-mantle boundary beneath the Comoros hotspot. *Geophysical Research Letters*, *27*(22), 3627–3630. https://doi.org/10.1029/2000gl011831

Wen, L., & Helmberger, D. V. (1998). Ultra-low velocity zones near the core-mantle boundary from broadband PKP precursors. *Science*, *279*(5357), 1701–1703. https://doi.org/10.1126/science.279.5357.1701

Wessel, P., Smith, W. H. F., Scharroo, R., Luis, J., & Wobbe, F. (2013). Generic mapping tools: Improved version released. *Eos, Transactions American Geophysical Union*, *94*(45), 409–410. https://doi.org/10.1002/2013EO450001

Wiens, D. (1997). Seismic experiment in Patagona and Antarctica. A broadband study of the tectonics and structure of the Antarctic Peninsula and Scotia Sea Regions [Dataset]. *International Federation of Digital Seismograph Networks*. https://doi.org/10.7914/SN/XB_1997

Wiens, D., Aster, R., & Bromirski, P. (2014). Collaborative research: Dynamic response of the Ross ice shelf to ocean waves and structure and dynamics of the Ross Sea from a passive seismic deployment on the Ross Ice Shelf [Dataset]. *International Federation of Digital Seismograph Networks*. https://doi.org/10.7914/SN/XH_2014

Wiens, D., & Nyblade, A. (2007). A broadband seismic experiment to image the lithosphere beneath the Gamburtsev Mountains, East Antarctica [Dataset]. *International Federation of Digital Seismograph Networks*. https://doi.org/10.7914/SN/ZM_2007

Wiens, D., Nyblade, A., & Aster, R. (2007). IPY POLENET-Antarctica: Investigating links between geodynamics and ice sheets [Dataset]. *International Federation of Digital Seismograph Networks*. https://doi.org/10.7914/SN/YT_2007

Williams, Q., & Garnero, E. J. (1996). Seismic evidence for partial melt at the base of Earth's mantle. *Science*, *273*(5281), 1528–1530. https://doi.org/10.1126/science.273.5281.1528

Williams, Q., Revenaugh, J., & Garnero, E. (1998). A correlation between ultra-low basal velocities in the mantle and hot spots. *Science*, *281*(5376), 546–549. https://doi.org/10.1126/science.281.5376.546

Wolf, J., Long, M. D., & Frost, D. A. (2024). Ultralow velocity zone and deep mantle flow beneath the Himalayas linked to subducted slab. *Nature Geoscience*. https://doi.org/10.1038/s41561-024-01386-5

Yu, S., & Garnero, E. J. (2018). Ultralow velocity zone locations: A global assessment. *Geochemistry, Geophysics, Geosystems*, *19*(2), 396–414. https://doi.org/10.1002/2017gc007281

Yu, S., Garnero, E. J., Shim, S. H., & Li, M. (2018). *Ultra-high velocity zones (UHVZs) at Earth's core mantle boundary, Abstract DI53A-0042*. American Geophysical Union.

Yuan, K., & Romanowicz, B. (2017). Seismic evidence for partial melting at the root of major hot spot plumes. *Science*, *357*(6349), 393–397. https://doi.org/10.1126/science.aan0760